AN ABSTRACT OF THESIS OF

Ahmad I. Abu-Dayah for the degree of Master of Science in Electrical and Computer Engineering presented on April 27,1993.

Title: Internal Charge-Phosphor Field Analysis, Electrical Characterization, and Aging Studies of AC Thin-Film Electroluminescent Devices.

Redacted for Privacy

Abstract approved: _____

Dr. John F. Wager

Three primary accomplishments are presented in this thesis. First, a new method developed to electrically characterize alternating-current thin-film electroluminescent (ACTFEL) devices, the internal charge versus phosphor field, (Q-F_p), technique. The Q-F_p technique provides direct information about the internal behavior of the ACTFEL device. The steady-state field, and internal conduction, polarization, leakage, and relaxation charges may be readily assessed from a Q-F_p curve. Second, electrical characterization of ZnS:Mn ACTFEL devices grown by atomic layer epitaxy (ALE) was performed subject to various waveforms; specifically the maximum applied voltage, V_{max}, the pulse width, PW, and the rise and fall times, RT/FT, are varied around their normal operating points and the electrical

response is monitored via the Q-F_p and capacitance-voltage (C-V) techniques. Changes in V_{max} lead to the largest changes in the electrical performance of the ACTFEL device. Such ALE ZnS:Mn ACTFEL devices exhibit polarity-dependent asymmetry which is attributed primarily to an asymmetry of the interface state density. Additionally, a polarity-dependent build-up of space charge in the ZnS is a secondary cause leading to the asymmetry properties of the ACTFEL device. Third, ging experiments are conducted using Q-F_p and C-V analysis. The aging characteristics are asymmetric with respect to the applied voltage pulse polarity. The presence of Cl at the lower interface and its tendency to migrate into the ZnS during aging is believed to be the major cause of the observed asymmetrical aging characteristics.

Internal Charge-Phosphor Field Analysis, Electrical Characterization, and Aging Studies of AC Thin-Film Electroluminescent Devices

by

Ahmad I. Abu-Dayah

A THESIS

submitted to

Oregon State University

in partial fulfillment of
the requirements for the
degree of

Master of Science

Completed April 27, 1993

Commencement June 1993

Approved:

Redacted for Privacy

Associate Professor of Electrical and Computer Engineering
in charge of major

Redacted for Privacy

Head of Department of Electrical and Computer Engineering

Redacted for Privacy

Dean of Graduate School

Date thesis is presented April 27, 1993

Typed by Ahmad I. Abu-Dayah

Bismillah arRahman arRaheem

I would like to dedicate this work to my mother, Kamleh, and my father, Ibrahim, who always encouraged me to succeed in my early studies.

Special thanks to my brother, Musa Abu-Dayah, without his help my undergraduate study would have been impossible.

I would also like to acknowledge my sisters Maryam, Huda, and Naderah, and my brothers Dr. Muhammed, Khalid, Jamal, Anwar, Ra'id, and Nader, who were always in my thoughts.

Finally, I would like to thank Jennifer L. Jones, without whom I would be a Master in Paper Science.

ACKNOWLEDGEMENTS

I would like to thank my advisor, Professor John F. Wager, for his advice, patience, and encouragement.

I would like to thank Professors S. M. Goodnick, A. Weisshar, and David Griffiths for serving on my committee.

Special thanks to Shiro Kobayashi, Allan Douglas, and Wie Ming Ang for many useful discussions.

Thanks to everyone at Planar Systems and Planar International specifically Ron Khormaei and Juha Viljanen for providing the samples used in this work.

This work was supported by the U.S. Army Research Office under contract D11L03-91G0242.

TABLE OF CONTENTS

LIST OF FIGURES

LIST OF TABLES

Internal Charge-Phosphor Field Analysis, Electrical Characterization, and Aging Studies of AC Thin-Film Electroluminescent Devices

CHAPTER 1-INTRODUCTION

Today, there is great interest in the development of full-color thin-film electroluminescent panels. The basic three colors required for full-color displays are red, green and blue. The potential of the rare earth ions to provide these basic three colors has led to intensive study of II-VI compounds in the past few years.[1] Electroluminescence (EL) is light emission from solid compounds generated by non-equilibrium charge carriers. In reference to the voltage applied, EL can be either low-or high-field. A typical low-field EL device is a light emitting diode in which carriers are injected via a p-n junction. High-field EL, on the other hand, is based on carriers accelerated up to energies large enough to excite EL luminescent centers.[2] The electric field required for high-field EL is on the order of megavolts per centimeter.

High-field EL systems can be divided into four groups; alternating-current (AC) or direct-current (DC) using powder samples or thin films.[3] Most current EL research and production is centered on AC thin-film electroluminescent (ACTFEL) devices.

Currently, ACTFEL devices are used for monochrome flat panel display applications.[4] ACTFEL devices have several

advantages, including size, resolution, brightness and viewing angle.

The first and most common EL phosphor discovered was ZnS:Mn, which gives a yellow emission. The preparation of thin-film materials emitting other colors has been one of the main goals in ACTFEL research in the 1980s. Furthermore, having a bright, stable luminescence for a long period of time (more than 10,000 hours) and meeting the high definition television (HDTV) standards are major objectives for ACTFEL displays.

The goal of this thesis is to investigate the aging instabilities of ZnS:Mn ACTFEL devices grown by atomic layer epitaxy (ALE). The changes associated with aging are assessed by monitoring various electrical parameters using the capacitance-voltage (C-V)[5,6]and the internal charge-phosphor field ($Q-F_p$)[7] techniques. The $Q-F_p$ technique is a new method for electrical characterization of ACTFEL devices. Furthermore, the electrical parameters are measured as a function of variation in the standard driving waveform; specifically, the maximum applied voltage, V_{max}, the pulse width, PW, and rise and fall time, RT/FT are varied around their normal operating values.

In Chapter 2, a review of relevant ACTFEL literature and a discussion of device operation are presented. Chapter 3 describes the experimental techniques used in this study, with particular emphasis on the new $Q-F_p$ technique. Chapter 4

includes electrical characterization of ACTFEL devices subject to variations in the applied voltage waveform. Chapter 5 presents an investigation of the aging instabilities and aging kinetics of ACTFEL devices. The final chapter contains the conclusions of this work as well as recommendations for future work. Some of the work presented here has been previously published or submitted for publication.[7-11]

CHAPTER 2-LITERATURE REVIEW OF ACTFEL DEVICES

2.1 HISTORY AND BACKGROUND

In the early 1900's, light emission from phosphor powders due to applied high electric fields was discovered. In 1936, the first EL structure was prepared by Destiau.[12] This structure contained two electrodes separated by a ZnS phosphor immersed in castor oil. In the late 1960's, electroluminescent studies of rare earth doped ZnS began and several colors from rare earth ions were obtained from ZnS:LnF3 thin films.[13] A great step forward in EL technology was the development of the double insulator MISIM (metal-insulator-semiconductor-insulator-metal) structure. In the early 1970's, Inoguchi et al[14] were very successful in maintaining a bright, stable luminescence for more than 10,000 hours using a MISIM device with a ZnS:Mn active layer. At the present time, ACTFEL devices have matured from laboratory experiments to commercial production. In fact, currently, 18-inch diagonal monochrome displays are in full production.

Most of the research today is focused on developing multi-color displays. Recently, two color (red and green) displays have been obtained.[15] The ability to generate the three primary colors has been demonstrated in several laboratories.[16-18] The major problem, however, is attaining a blue phosphor with enough brightness and intensity. It is expected that a full-color display will be demonstrated by early 1993.

2.2 PREPARATION OF ACTFELS AND STRUCTURES

Preparation of ACTFEL devices is accomplished by one of two major process techniques; physical vapor deposition (PVD) or chemical vapor deposition (CVD). PVD includes sputtering and evaporation while CVD includes metal-organic chemical vapor deposition (MOCVD) and atomic layer epitaxy (ALE).

Sputtering [19] is a process in which a stream of gas ions transfers its kinetic energy to a target material. Target atoms are then sputtered (ejected) from the target surface onto a solid substrate, where they condense as a thin film. Evaporation, on the other hand, is obtained from resistance, electron beam, radio frequency or laser heated sources.[20,21] The crystallinity of films prepared by PVD is usually improved by annealing the films at elevated temperatures.

MOCVD is a process in which reactions of organometallic compounds are utilized at atmospheric or reduced pressures. MOCVD process is more often used to prepare III-V semiconductors rather than II-VI EL phosphors.[19] The ALE technique is one of the most successful growth methods used in the commercial production of ACTFEL devices.[22,23] ALE processes depend upon exchange reactions between gaseous reactants chemisorbed onto a substrate surface.

The ALE process for ZnS deposition itself is established by first exposing the substrate to a Zn-containing source gas, such as zinc-chloride ($ZnCl_2$) and then purging with a nonreactive gas such as N_2 so that only one monolayer of Zn is

left on the surface. In this step, several issues should be considered in order to meet the desired thickness and smoothness of the grown layer such as the nature of gas used, pressure, dwell time, flow rate and substrate temperature. The next step is to expose the substrate to a S-containing ambient such as hydrogen sulfide (H_2S). Finally, in a similar manner, the excess S is purged. The ALE devices used in this study are fabricated using $ZnCl_2$ and H_2S process gases. The ALE process determines several of the phosphor properties of importance for ACTFEL devices such as crystal structure,[24] optical properties, and the uniformity of the thin film thickness over the device area.

The ACTFEL device structure used for this study is shown below in Fig. 2-1.

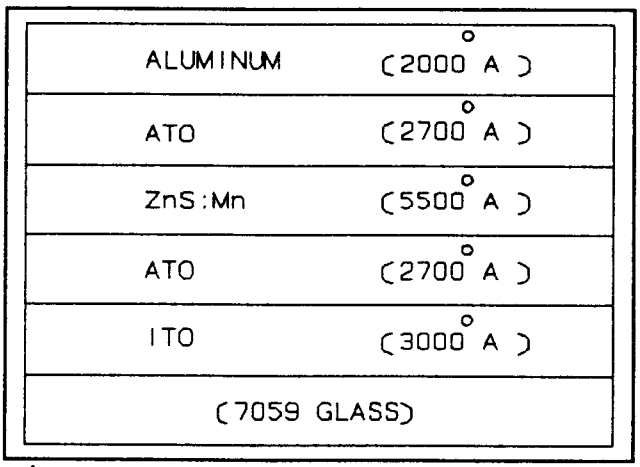

Figure 2-1: ACTFEL structure and dimensions used in this study.

The ACTFEL devices are fabricated at Planar International and grown by ALE. As shown in Fig. 2-1, the phosphor layer is sandwiched between two insulators made of aluminum titanium

oxide (ATO). The whole device is then sandwiched between two layers, Al and indium tin oxide (ITO), which are used for electrical contacts.

2.3 DEVICE OPERATION

ACTFEL devices operate by applying an AC bias to the electrodes. The standard waveform used in this work to drive ACTFEL devices is symmetric with alternating bipolar pulses of trapezoidal shape with 5 μs rise and fall times and a pulse width of 30 μs. The frequency of the waveform is 1 kHz. The typical amplitude of the waveform is about 40 volts above the threshold voltage. A schematic for this driving waveform is shown in Fig. 2-2.

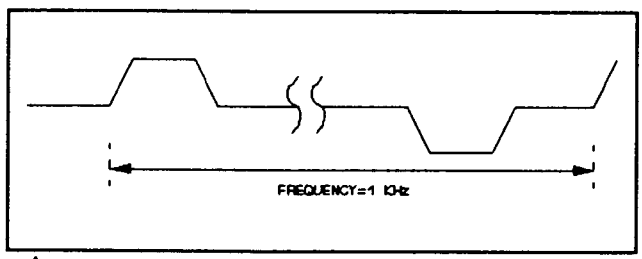

Figure 2-2: ACTFEL standard driving waveform.

Once a bias is applied to the electrodes of the ACTFEL device, the voltage dropped across the ACTFEL device divides across the insulator and phosphor capacitors until breakdown occurs. At this point, the voltage drop across the phosphor layer has an associated field which produces a large number of electrons, via tunnel emission from interface states, some of which are sufficiently hot to excite luminescent impurities which subsequently radiatively recombine, giving off light.

Further increases in the applied voltage results in an increase in the conduction charge which gives higher luminescence.

Perhaps, a better explanation of ACTFEL device operation is obtained through the use of energy band diagrams. An equilibrium energy band diagram of an ideal ACTFEL device is shown in Fig. 2-3. Application of a positive bias to the Al

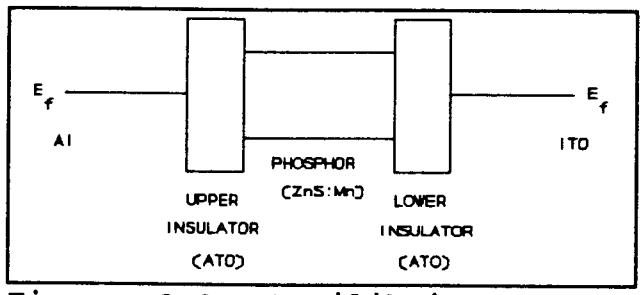

Figure 2-3: Equilibrium energy band diagram for an ideal ACTFEL device.

electrode of the ACTFEL device results in the situation shown in Fig. 2-4. The charges indicated in Fig. 2-4 are set up by the previous, negative voltage pulse. As seen in Fig. 2-4, an internal phosphor field (F_{pol}) exists due to the accumulation of charge on the interface from the previous pulse. F_{pol} adds to the external applied field, (F_{ext}), until tunnel emission from interface states occurs, resulting in the onset of conduction current. At this point, the phosphor field (F_p) may be clamped due to a large number of electrons that tunnel-emit from interface states. After removing the bias (i.e F_{ext}= 0), the polarity of F_{pol} is reversed as shown in Fig. 2-5. This is simply explained by Kirchhoff's voltage law where the sum of

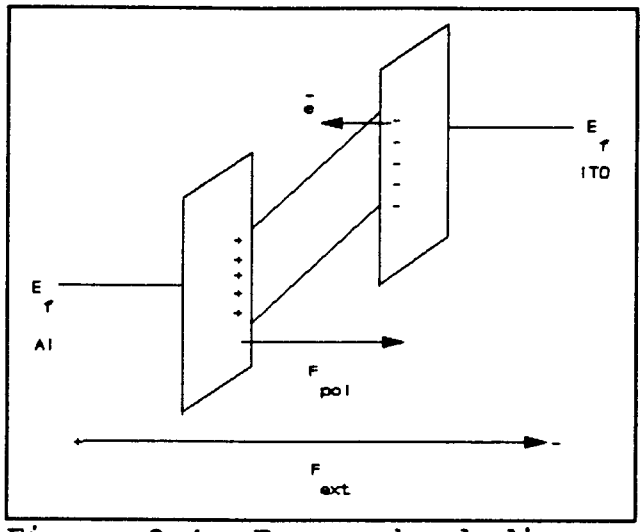

Figure 2-4: Energy band diagram for a positive bias applied to the Al electrode of an ACTFEL device.

voltages must equal zero (i.e $V_{ph}+V_I=V_{ext}=0$) where V_{ph} is the voltage across the phosphor, V_I is the voltage across the insulators, and V_{ext} is the external applied voltage). As seen in Fig. 2-5, some electrons can tunnel out of the more shallow interface states if F_{pol} is large. This is a drawback for ACTFEL device operation since fewer electrons remain at on

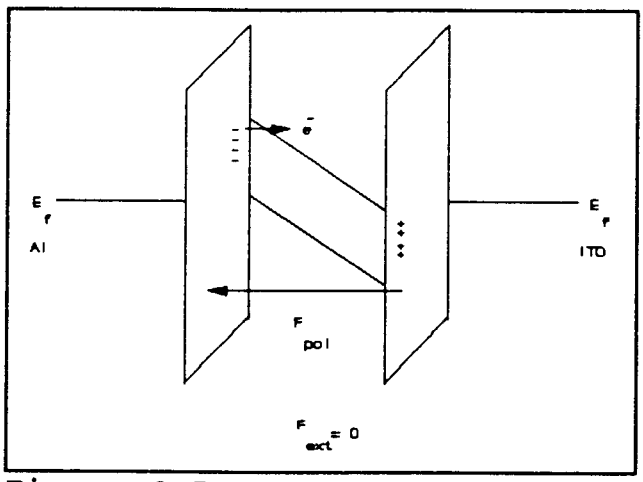

Figure 2-5: ACTFEL energy band diagram after removing the bias.

the interface requires more applied bias for the next pulse.

Applying a negative bias to the ACTFEL device adds to F_{pol}; thus, if F_{pol} is large, less external bias is needed for electrons to tunnel-emit from interface states. This step is

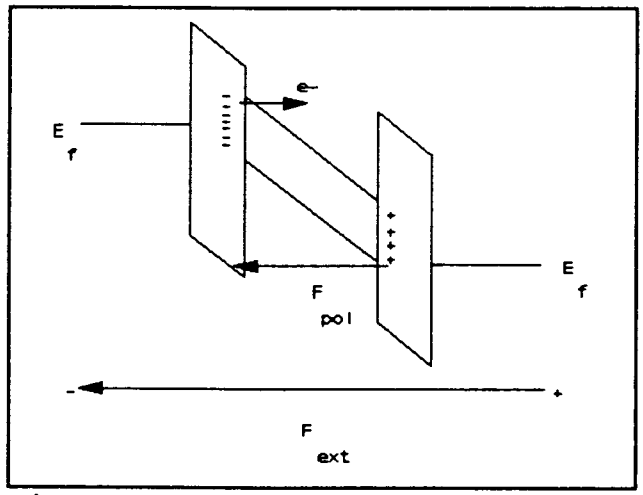

Figure 2-6: Energy band diagram for a negative bias applied to the Al electrode for an ACTFEL device.

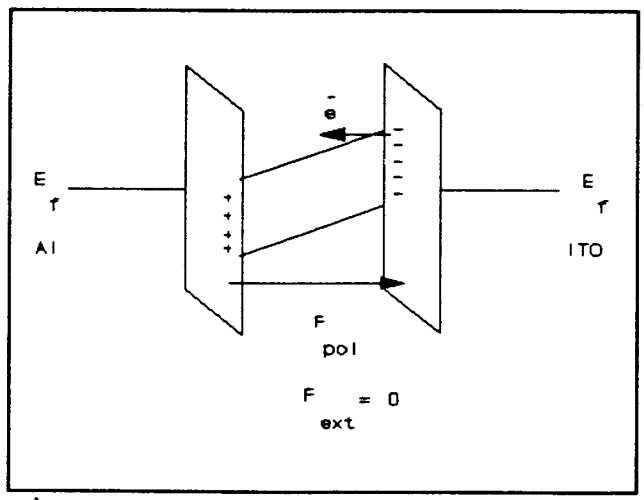

Figure 2-7: ACTFEL energy band diagram after removing the negative applied pulse.

shown in Fig. 2-6 in which the slopes of the energy bands are

reversed (i.e negative slopes). After removing the negative applied bias, the polarity of F_{pol} is reversed, as shown in Fig. 2-7.

2.4 PREVIOUS ACTFEL DEVICE AGING STUDIES

The aging characteristics and device stability of ACTFEL flat-panel displays have been the subject of numerous studies.[26-31]The majority of this work has focused on monitoring the brightness or luminescence versus voltage (B-V) of the ACTFEL device as a function of aging time. Another approach is to monitor the electrical characteristics of ACTFEL devices in order to study the electrical properties of ACTFEL devices.

B-V aging studies are important for assessing the optical behavior of ACTFEL devices. These studies enable researchers to draw some conclusions about the ACTFEL device stability and to develop device strategies to improve the ACTFEL aging characteristics. Improving the ACTFEL device stability is usually achieved by changing the process methods used to fabricate the device or by exploring different materials to be used in the process. Examples of such approaches are discussed next.

Workers at Sharp[31] have used the B-V characteristics to examine the device stability of ZnS:Mn ACTFEL devices grown by halide-transport chemical vapor deposition (HTCVD) which have aging properties identical to ACTFEL devices grown by vacuum evaporation and ALE. The B-V characteristics of evaporated and

ALE ZnS:Mn ACTFEL devices show completely different aging mechanisms. Sharp workers found that the aging pattern exhibited in evaporated devices has a positive shift in the B-V curves to higher threshold voltages while the ALE devices exhibited a negative shift to lower threshold voltages. They conclude that the shift between positive and negative is due to the growth temperature used during HTCVD growth. For vacuum evaporation, the growth temperature is less than 200°c while ALE growth occurs at about 500°c. The negative shift is explained as a combination of a softening and a shifting in the B-V curve, which are attributed to an asymmetric polarization charge and band bending in the ZnS layer, respectively. On the other hand, the positive shift is attributed to bulk-limited conduction, in which case the emission would be symmetric.

Workers at Planar Systems and Oregon State University[28,29] have tried to improve the stability of their ACTFEL devices by adding a CaS layer at one or both of the phosphor-insulator interfaces. Another approach they tried involved oxygen exposure of the ZnS layer prior to the second insulator deposition. The conclusion of their work is that both approaches improve ACTFEL device stability. However, the second approach reduces the brightness of the device. Their explanation of the improved stability of ACTFEL device is associated with a reduction in the tendency of sulfur vacancies to diffuse during device operation.

Workers at Lohja and Helsinki University of Technology[27] performed aging studies by monitoring the B-V characteristics of devices grown by ALE. The ALE devices studied have an Al_2O_3-ZnS:Mn-Al_2O_3 structure sandwiched between two sputtered ITO layers. They conclude that the aging process is due to electron trapping at the ZnS:Mn insulator interface. Electron trapping increases as aging time increases. Also, the shift in the B-V curves to lower threshold voltages with aging time is attributed to trapping at the ZnS:Mn insulator interface.

A second approach for studying ACTFEL device aging is to monitor the electrical characteristics of ACTFEL devices as a function of aging time. Recently, Davidson[4,30] performed aging studies of ZnS:Mn ACTFEL devices grown by vacuum evaporation. These experiments were performed for 45 hours by monitoring the C-V and Q-V characteristics. Davidson observed that the insulator and phosphor capacitances are constant with respect to aging time. These observations indicate that the electrostatic charge distribution responsible for aging occurs near the phosphor/insulator interface. He also observed that the C-V curves shift rigidly to higher turn-on voltages with aging time. This indicates that degradation of the ACTFEL device is due to changes in the fixed charge and not the interface state charge. From these observations, an aging model for evaporated ZnS:Mn ACTFEL devices is provided to explain the aging of these devices. This model suggests that[27] the formation of deep level, fixed charge states is a result

of atomic rearangement at the insulator/phosphor interface where electrons are trapped and give rise to a reduction in the conduction charge.

2.5 PREVIOUS ACTFEL DEVICE ELECTRICAL CHARACTERIZATION.

Electrical characterization of ACTFEL devices is generally accomplished via Q-V, C-V, and current-voltage (I-V) analysis. Additionally, SPICE modelling may be used to electrically characterize the ACTFEL device. Previous work involving these techniques and SPICE modelling has been performed by several authors.[26,32] Davidson et al. have performed an electrical characterization of evaporated ZnS:Mn ACTFEL devices using C-V and Q-V analysis and have deduced a SPICE model that accounts for the experimental results.[26] The SPICE model is shown in Fig. 2-8. R_{ito} represents the resistance of the ITO layer. R_{i1} and C_{i1} represent the resistance and the capacitance of the lower insulator, respectively. C_p and R_p represent the capacitance and resistance of the phosphor layer, respectively. R_d is referred to as a diode or hot electron resistor; it is used to model tunneling from interface states. The back-to-back Zener diodes (i.e., D1 and D2) are used to characterize the breakdown voltage of the phosphor layer. C_{i2} and R_{i2} are the capacitance and resistance of the upper insulator layer, respectively.

C-V analysis and SPICE modelling have provided valuable information about the internal device physics of evaporated

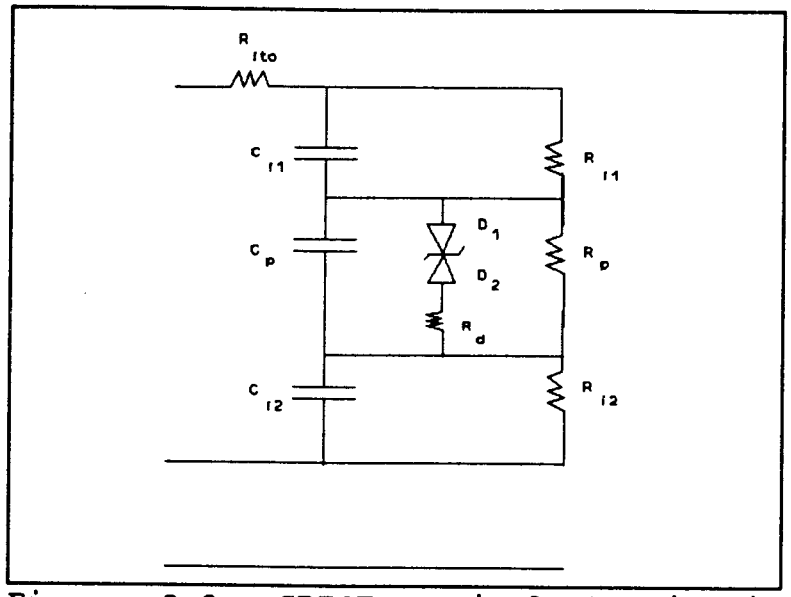

Figure 2-8: SPICE equivalent circuit model.

ZnS:Mn ACTFEL devices. The conclusion of Davidson's work is that the capacitance rise near zero voltage is due to a non-zero value of R_{ito} which gives rise to a simple RC effect. Also, the abruptness of the C-V curve is very sensitive to R_d but also depends on R_{ito}. Finally, a second small capacitance rise in the insulator capacitance regime of the C-V curve depends strongly on R_{ito} and R_d but shows very little dependence on the insulator or phosphor resistances.

Further electrical characterization and modelling of ACTFEL devices has been reported by Douglas and Wager[32]. These experiments were also performed using evaporated ZnS:Mn ACTFEL devices. This work involved a variation of the standard driving waveform and its effect on the electrical properties of the ACTFEL device. Also, SPICE simulation was used for comparison with the experimental results. The SPICE model

used was a refinement of Davidson's SPICE model. The refined SPICE model includes a resistor and capacitor in parallel which are in series with R_d. These two additional parameters are believed[32] to be associated with hot electron emission. This refined SPICE model provided simulated electrical trends which are in excellent agreement with experimental results. Systematic variations in the applied voltage waveform show that the variations in the maximum applied voltage (V_{max}) have the strongest effect on the measured or simulated electrical properties while rise and fall time (RT/FT) variations have the least effect and pulse width (PW) variations have an intermediate effect.

CHAPTER 3-EXPERIMENTAL TECHNIQUES

3.1 INTRODUCTION

The standard methods used to characterize the electrical properties of ACTFEL devices by are Q-V[31] and C-V analysis.[4,5,6] The Q-V method may be used to determine many external and internal electrical parameters such as the turn-on voltage, conduction and polarization charges, and insulator and phosphor capacitances. Analysis of a C-V curve can be used to establish different turn-on voltages and the interface state density in the pre-clamping regime. In this thesis, a new technique, the Q-F_p[7] method is presented as a means of determining the internal behavior of ACTFEL devices.

Section 3.2 discusses the general techniques used for electrical characterization of ACTFEL devices. Section 3.3 presents the new Q-F_p technique while section 3.4 includes examples of Q-F_p applications. The final section contains a summary of this chapter.

3.2 GENERAL EXPERIMENTAL TECHNIQUES

As mentioned in the introduction, C-V and Q-V analysis are the conventional methods used to electrically characterize ACTFEL devices. Electrical characterization using these two techniques is accomplished using the circuit shown in Fig. 3-1. Figure. 3-1 consists of an IBM 286 compatible computer (Iconix model) that has a GPIB capability. The computer controls an arbitrary waveform generator (Wavetek model 275) which provides a 1 Khz waveform of symmetric bipolar pulses.

An RC filter with a cut-off frequency of 50 kHz to 50 MHz range is placed in series with the waveform generator to eliminate some noise associated with the waveform. An amplifier (Apex model PA-85) with a gain of approximately 40 is connected at the output of the RC filter to amplify the signal. A series resistor, R_s, of magnitude 200 ohms and a sense element which could be either a resistor or a capacitor are connected in series with the ACTFEL device. Additionally, the computer controls a digitizing oscilloscope (Tektronix model 7854).

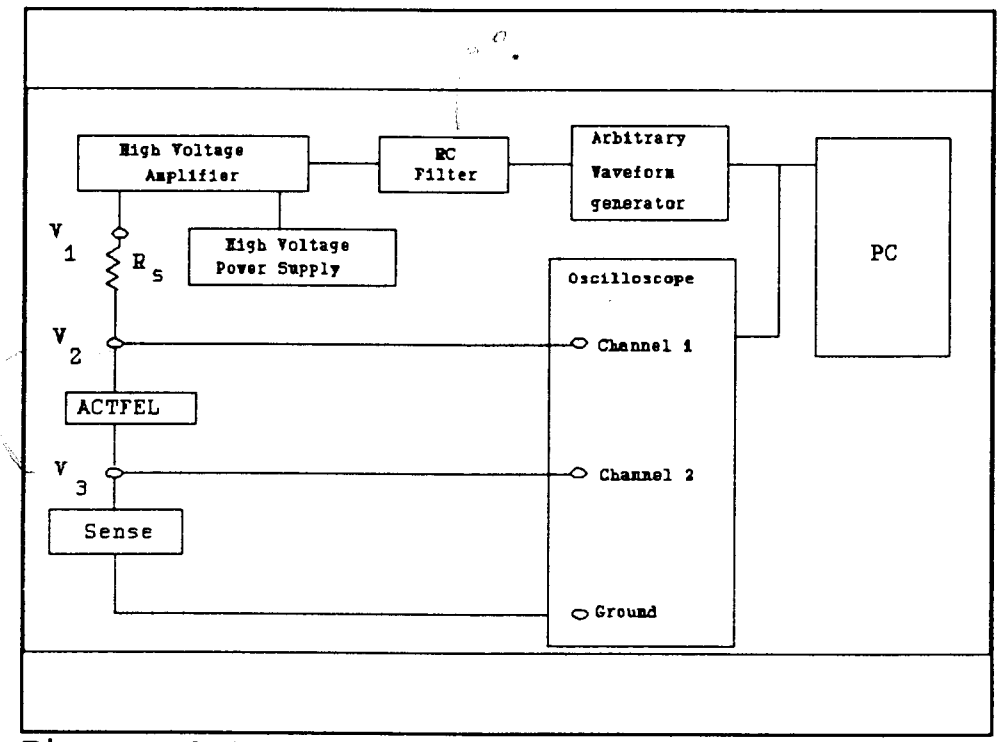

Figure 3-1: System set-up used for ACTFEL electrical characterization.

C-V analysis is accomplished[4,5,6] using a resistor, R_c, as a sense element and the C-V curve is obtained by plotting the dynamic capacitance as a function of the voltage across the

ACTFEL device, $C(V_2-V_3)$, given by

$$C(v_2-v_3)=\frac{i(t)}{\frac{d}{dt}[v_2(t)-v_3(t)]} \tag{1}$$

versus the voltage across the ACTFEL device $[v_2(t)-v_3(t)]$. The current, $i(t)$, is obtained from the voltage across the current sense resistor

$$i(t)=\frac{v_3(t)}{R_c} \tag{2}$$

A typical C-V curve for an ALE ZnS:Mn ACTFEL device is shown in Fig. 3-2. The C-V plot shown in Fig. 3-2 can provide much valuable information about the ACTFEL device. The

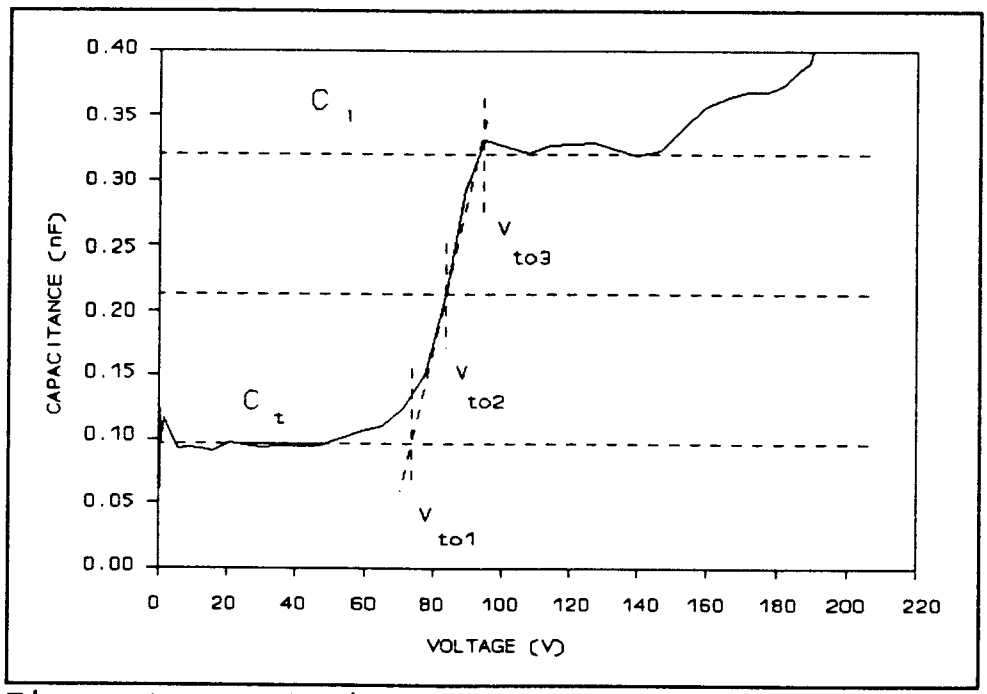

Figure 3-2: A typical C-V curve for an ALE ZnS:Mn ACTFEL device under an applied bias of 210 V.

insulator capacitance, C_i, total capacitance, C_t, as well as

three different turn-on voltages are easily measured. The three turn-on voltages, V_{to1}, V_{to2}, and V_{to3} as indicated are defined for different regimes. V_{to1}, corresponds to the initiation of electron emission from interface states whereas V_{to3} is associated with field clamping or the attainment of a steady-state field in the phosphor.[5] V_{to2} is the turn-on voltage at which the onset of conduction in the phosphor occurs.

Q-V analysis is accomplished by using a capacitor, C_s, as the sense element in Fig. 3-1 and by acquiring $v_2(t)$ and $v_3(t)$ using a digitizing oscilloscope (Tektronix model 7854). The external charge, $q^e(t)$, is then plotted versus $v_2(t)-v_3(t)$ where

$$q^e(t) = C_s v_3(t) \tag{3}$$

A typical Q-V curve for an ALE ZnS:Mn ACTFEL device is shown in Fig. 3-3. The turn-on voltage, V_{to}, corresponds to to the V_{to2} in C-V analysis. Many of the Q-V characteristics are discussed in the next section as it is important to compare Q-V and Q-F_p characteristics.

3.3 INTERNAL CHARGE-PHOSPHOR FIELD (Q-F_p) TECHNIQUE

The Q-F_p technique is presented as a method for characterization of the electrical properties of ACTFEL devices. Q-F_p analysis provides direct information about the internal behavior of the ACTFEL device. Q-F_p analysis is accomplished using the circuit shown previously in Fig. 3-1

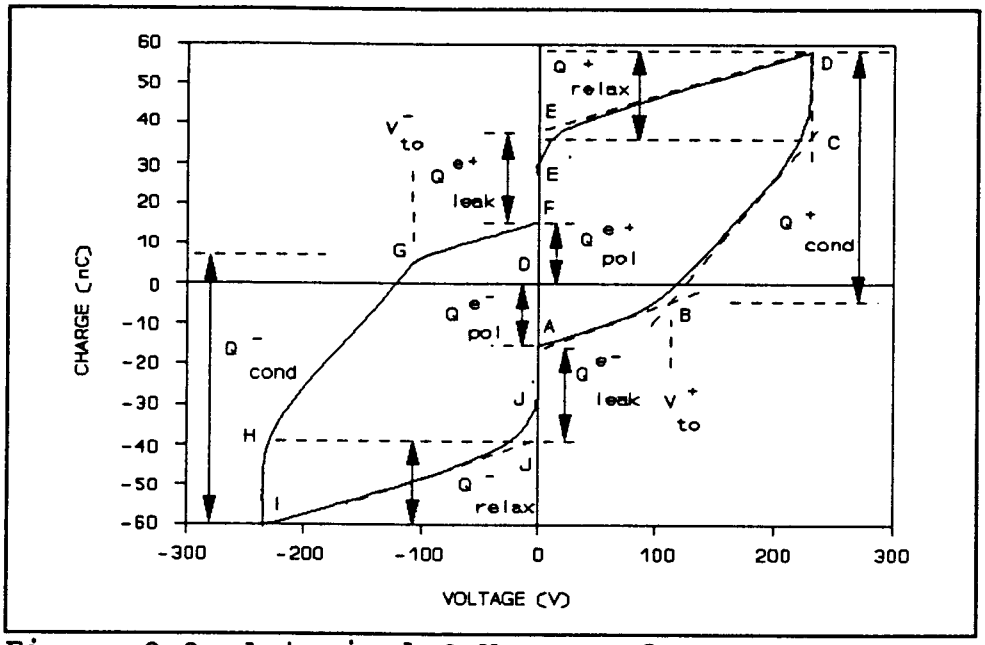

Figure 3-3: A typical Q-V curve for an ALE ZnS:Mn ACTFEL device.

where the sense element is a capacitor as in the case for Q-V analysis. The equations used to generate a Q-F_p plot are as follows. The internal phosphor field, $F_p(t)$, is defined from Eq.(2b) of Brinquier's paper[36] and given by

$$F_p = \frac{Q - C_i V_g}{d_p (C_i + C_p)} \tag{4}$$

where d_p is the phosphor field thickness and C_i and C_p are the insulator and phosphor capacitances, respectively. V_g is the external applied voltage across the ACTFEL device. V_g is evaluated as shown in Fig. 3-1 and is given by

$$V_g = v_2(t) - v_3(t) \tag{5}$$

Q is the internal charge in the phosphor and is defined from Eq.(4) of Brinquier's paper[36] as

$$Q = \frac{(C_i + C_p)}{C_i} Q_a - C_p V_g \tag{6}$$

where Q_a is the external charge and is also found from Fig. 3-1 as

$$Q_a = C_s v_3(t) . \tag{7}$$

Substituting Eqs.(5) and (7) into Eq.(6), the internal charge, Q, which is denoted as q(t) since it is a function of time, becomes

$$q(t) = \frac{(C_i + C_p)}{C_i} C_s v_3(t) - C_p [v_2(t) - v_3(t)] . \tag{8}$$

Substituting Eqs.(5) and (8) into Eq.(4), the internal phosphor field, $F_p(t)$, becomes

$$F_p(t) = \frac{1}{d_p}\left[\frac{C_s V_3(t)}{C_i} - (v_2(t) - v_3(t))\right]. \tag{9}$$

A Q-F_p curve is obtained by plotting q(t) versus $F_p(t)$, as assessed from Eqs.(8) and (9), respectively.

A Q-F_p curve for an evaporated ZnS:Mn ACTFEL device with sputtered SiON insulators is shown in Fig. 3-4. The labels A through J are used to designate certain points on the Q-F_p curve; these points are also shown on a corresponding Q-V curve, as indicated in Fig. 3-5. Superscripts + and - used in Figs. 3-4 and 3-5 correspond to the polarity of the applied voltage pulse; a positive voltage pulse is defined as when the Al electrode bias is positive. Various fields and charges may

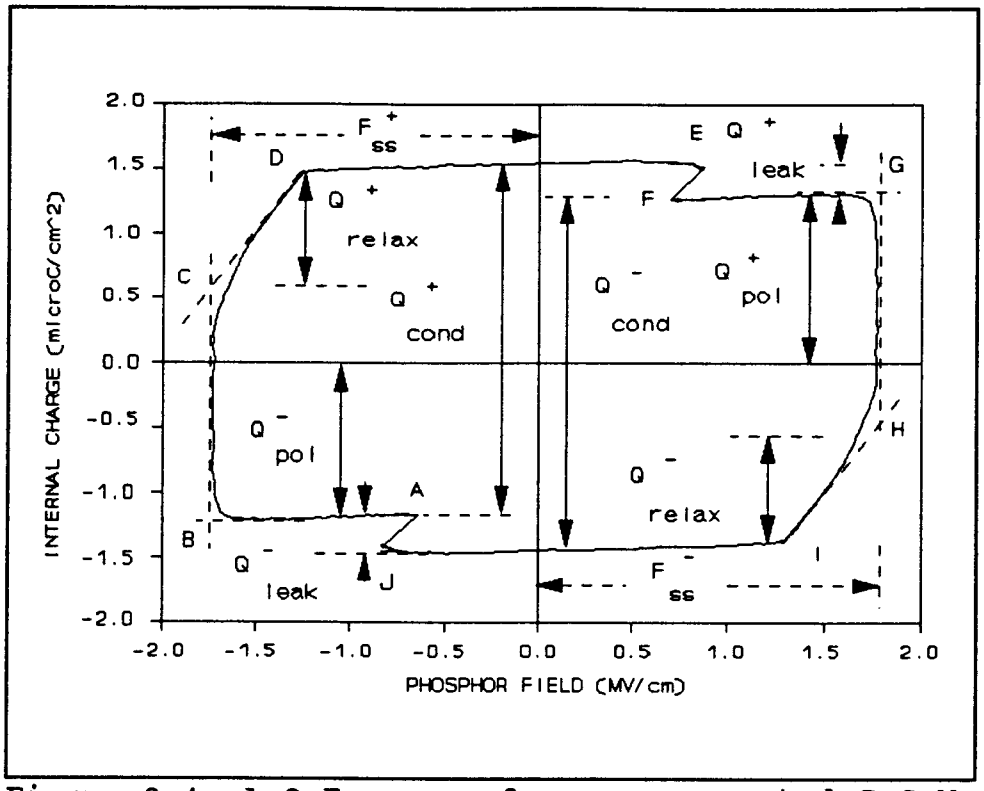

Figure 3-4: A Q-F_p curve for an evaporated ZnS:Mn ACTFEL device with sputtered SiON dielectrics. The applied voltage amplitude is 240 v.

be evaluated from the Q-F_p curve as follows. F_{ss}, the steady-state field, corresponds to the phosphor field which is approximately constant during a portion of the applied voltage wavefrom in which the external bias is rising. Q_{cond} is the conduction charge transported across the phosphor during the voltage pulse; this is the charge responsible for impact excitation of luminescent impurities and, hence, which gives rise to light emission. Q_{pol} is the polarization charge stored at the phosphor/insulator interface just prior to the onset of the subsequent pulse of opposite polarity. Note that Q_{pol} is defined with an "e" superscript in the Q-V curve of Fig. 3-5

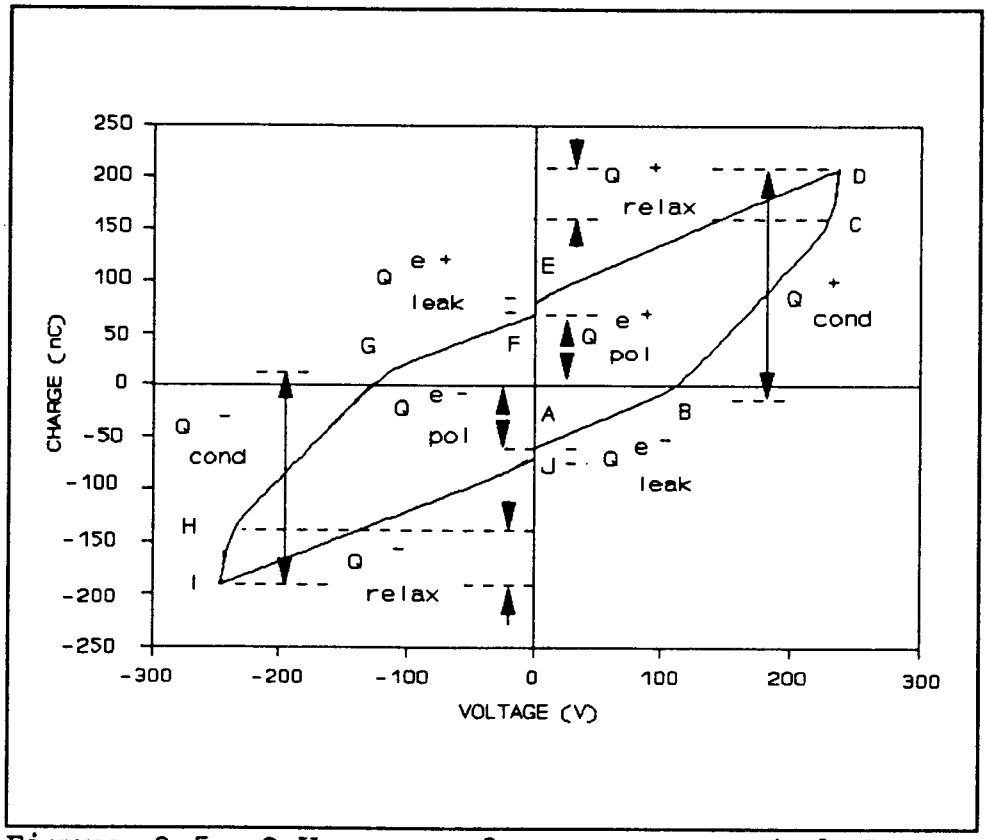

Figure 3-5: Q-V curve for an evaporated ZnS:Mn ACTFEL device with sputtered SiON dielectrics.

in order to distinguish this charge as an external charge. No "e" superscript is required in a Q-F_p curve since all of the charges are internal. Q_{leak} denotes the leakage charge arising from the emission of electrons from shallow interface states[26,8] during the zero voltage portion of the waveform. Finally, Q_{relax} is the relaxation charge[32] which flows across the phosphor during the portion of the wavefrom at which the applied voltage is constant at its maximum value; the phosphor field relaxes during this period of the waveform, hence the identification as relaxation charge.

In order to further clarify the features of a Q-F_p curve,

an explanation of the curve from A to F is now provided. The point labeled A in Fig. 3-4 corresponds to the onset of a positive voltage pulse applied to the Al electrode. Non-zero values of Q and F_p are observed at A because of the polarization charge residing at the phosphor/insulator interface left behind by the previous pulse of opposite polarity. The AB portion of the Q-F_p curve arises from the rising edge of the external voltage pulse when the magnitude is less than that required for turn-on of the ACTFEL device. BC also occurs during the rising portion of the external voltage pulse but the voltage magnitude is greater than the turn-on voltage for the BC portion of the Q-F_p curve; the field is constant during much of this portion of the waveform and is equal to F_{ss}. CD corresponds to the portion of the waveform in which the external voltage is held constant at its maximum amplitude. Section DE of the Q-F_p curve is obtained during the falling edge of the voltage pulse; the polarity of the phosphor field reverses during this portion of the waveform. EF corresponds to the segment of the waveform in which no external bias is applied to the ACTFEL device. The remainder of the Q-F_p curve from F to A is similar to A to F portion of the curve just described except that the external applied voltage is of opposite polarity.

In the Q-F_p technique, q(t) and $F_p(t)$ both depend on C_i, as indicated in Eqs.(8) and (9). Thus the accuracy of a Q-F_p curve depends upon how well C_i is established. Typically, the

value of C_i employed is calculated from the known thicknesses and dielectric constants of the insulator layers. These calculated values of C_i are compared to C_i measured from C-V curves and are found to be in good agreement for evaporated ZnS:Mn ACTFEL devices but do not always agree with those of ALE ZnS:Mn ACTFEL devices. The measured values of C_i for ALE devices tend to be greater than the expected from the calculated values as will be discussed in chapter 4.

The dependence of Q-F_p on C_i is investigated for an evaporated ACTFEL device in which the actual value of C_i is well-established as shown in Figs. 3-6 and 3-7. As seen, the Q-F_p characteristics are changed or deformed as C_i is varied. Additionally, the Q-F_p characteristics are investigated varying C_p since q(t) depends on C_p (see Eq.(8)). Q-F_p curves as a function of variations in C_p are shown in Figs. 3-8 and 3-9. The results of varying C_i and C_p on the Q-F_p curve are summarized in Table 3-1 and discussed next.

Under- or over-estimating C_i by 5% or more changes the magnitude of the charge and field measured. For example, sections AB/FG, where Q_{pol} is measured, are no longer constant, horizontal lines but vary in a linear fashion as shown in Fig. 3-6 and 3-7; this non-horizontal variation is non-physical and, therefore, indicative that C_i or C_p have not been accurately estimated. Similarly, sections DE/IJ, in which Q_{cond} is evaluated and in which the external applied voltage decreases from V_{max} to zero volts, are no longer constant,

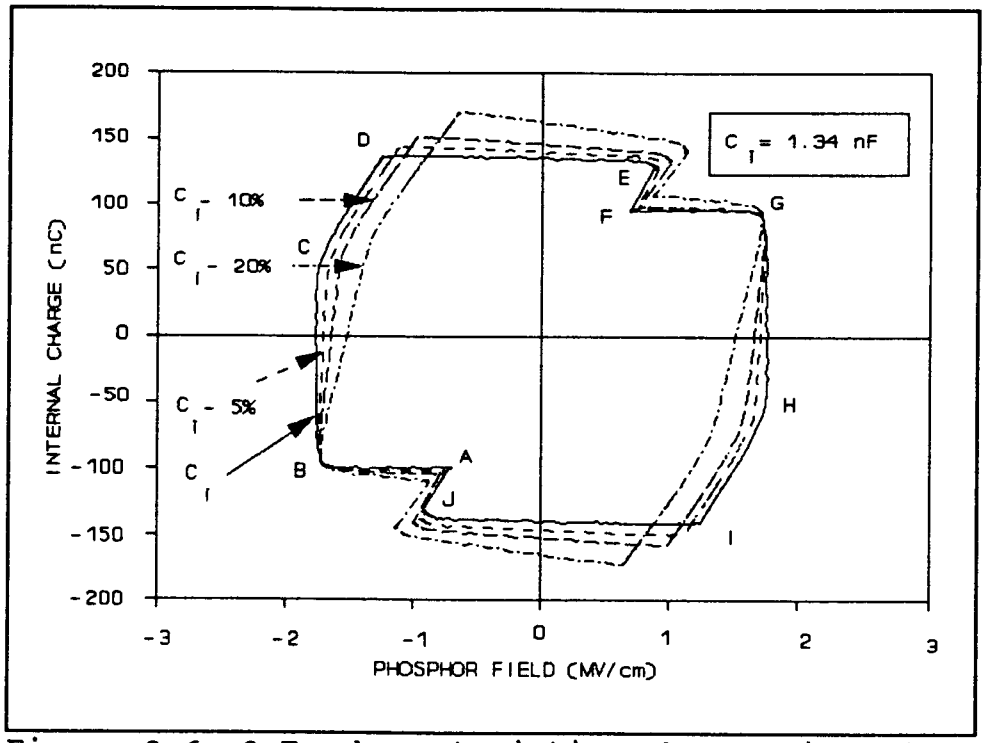

Figure 3-6: Q-F_p characteristics when C_i is under-estimated.

horizontal lines but change in a linear fashion with increasing slope for larger values of C_i; again, this behavior is non-physical and indicative that C_i or C_p have not been accurately estimated. Sections BC/GH, in which F_{ss} is evaluated, shift non-rigidly to higher or lower values away from the constant, vertical line obtained when the actual C_i is used. Sections CD/HI, where Q_{relax} is evaluated, do shift as well but the value of Q_{relax} is unchanged since the change in charge at points C/H and D/I is equivalent. Similarly, sections EF/JA, in which Q_{leak} is calculated exhibit rigid shifts so that Q_{leak} does not change. Note that F_{ss} is not effected by the value of C_p employed whereas it is sensitive to C_i.

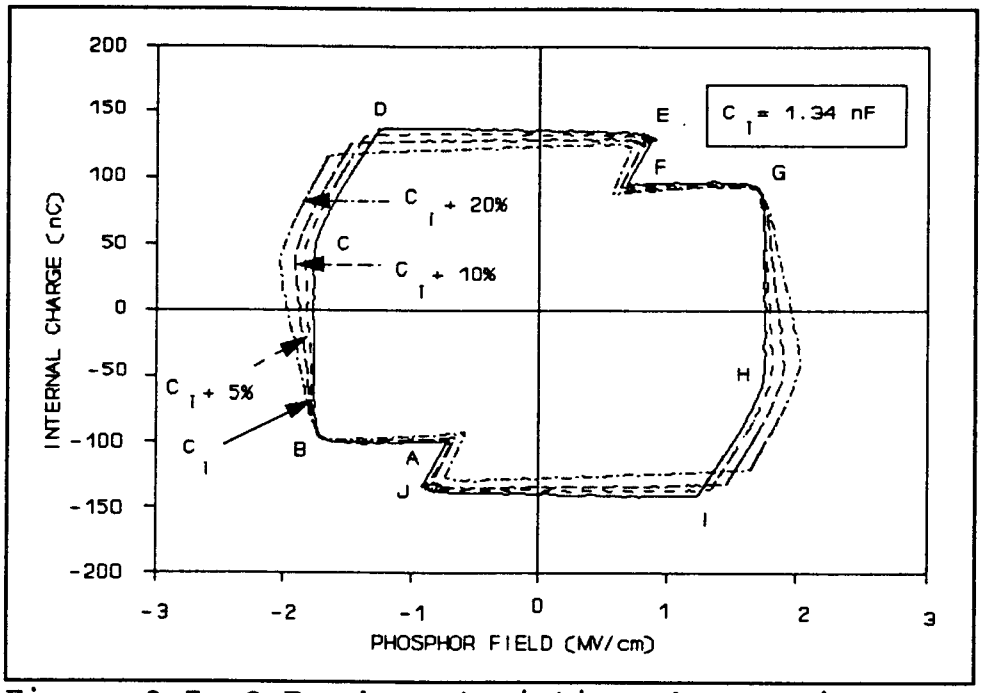

Figure 3-7: Q-F_p characteristics when C_i is over-estimated.

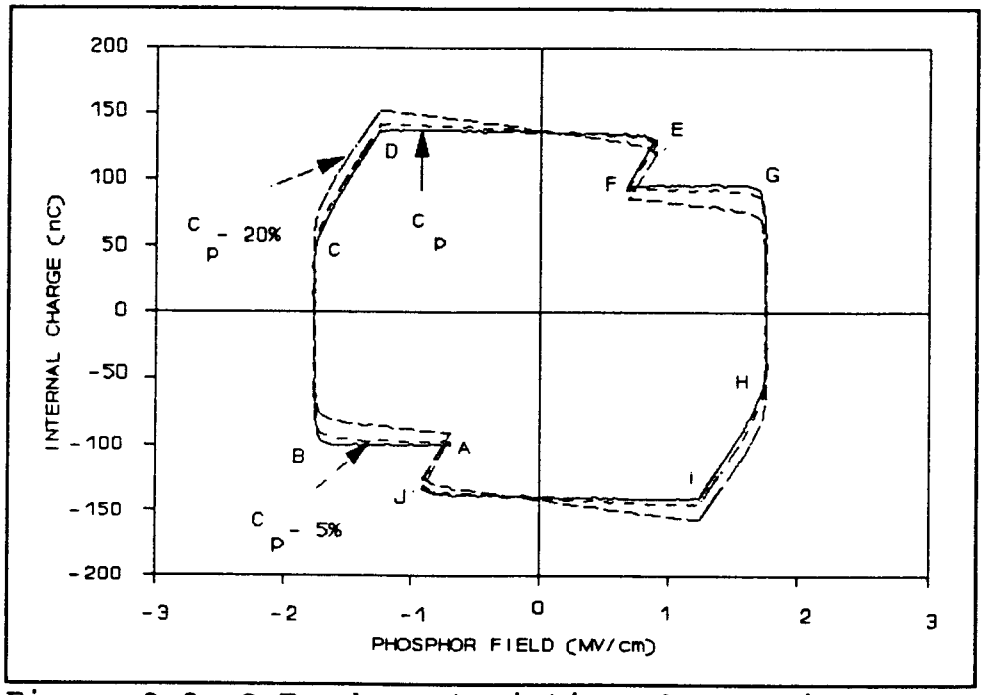

Figure 3-8: Q-F_p characteristics when C_p is under-estimated.

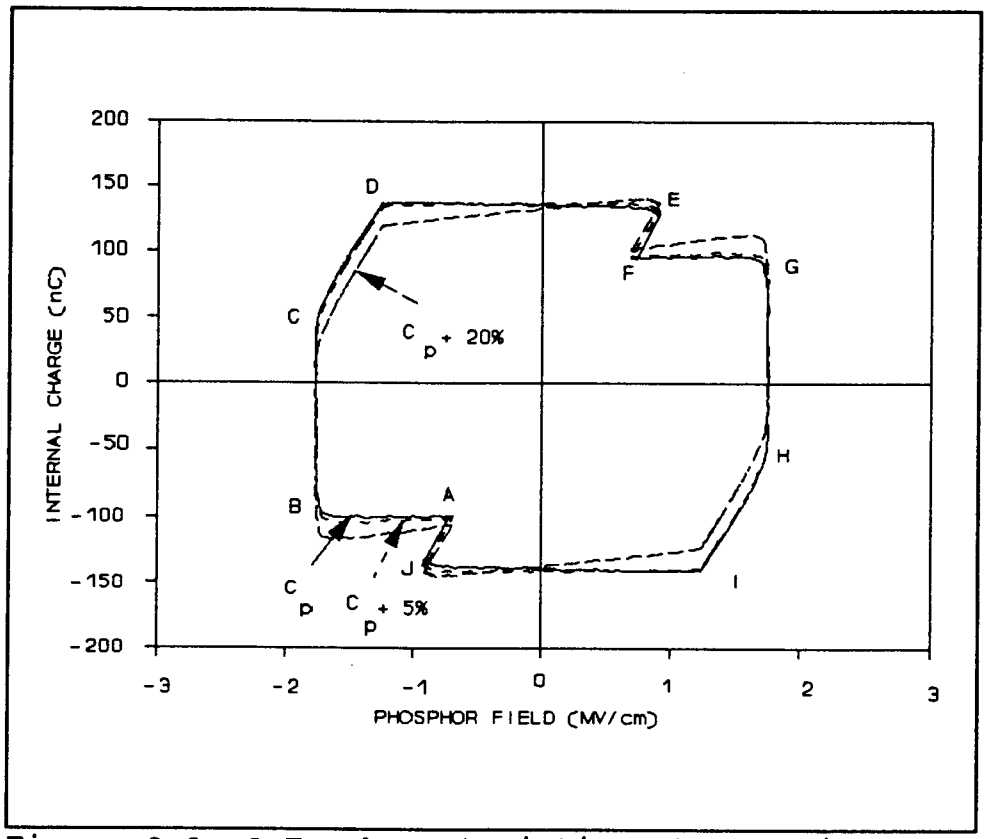

Figure 3-9: Q-F_p characteristics when C_p is over-estimated.

It is often difficult to accurately estimate C_i for ALE ACTFEL devices which exhibit strong field-clamping. An alternative procedure for assessing C_i is to plot a family of Q-F_p curves as a function of C_i and to choose C_i based on the value of C_i which yields the most horizontal AB/FG and DE/IJ sections of the Q-F_p curve. This technique for estimating C_i is employed in chapters 4 and 5 where C_i is assessed as a function of V_{max}, PW, RT/FT and aging time. Note that since C_i depends on various waveform parameters and aging time, it is more appropriate to refer to C_i as an "effective" insulator capacitance.

Table 3-1: A summary of C_i and C_p values and their Q-F_p variations.

C_i or C_p	Q-F_p sections				
	AB/FG	BC/GH	CD/HI	DE/IJ	EF/JA
Measured C_i and C_p	flat	flat vertical	increase	flat	decrease
C_i+error error>5%	decrease	shift to higher F_{ss}	see Fig.3-7	increase	see Fig.3-7
C_i-error error>5%	increase	shift to lower F_{ss}	see Fig.3-6	decrease	see Fig.3-6
C_p+error error>5%	decrease	no change	see Fig.3-9	increase	see Fig.3-9
C_p-error error>5%	increase	no change	see Fig.3-8	decrease	see Fig.3-8

3.4 Q-F_p EXAMPLES

The utility of the Q-F_p technique can be demonstrated by comparing Q-F_p characteristics for several devices. As an example, Q-F_p curves are compared in Fig. 3-10 and Table 3-2 for ZnS:Mn ACTFEL devices grown by evaporation with SiON insulators or by ALE with ATO insulators. For comparison purposes, V_{max} was chosen to be approximately 60 V above threshold (i.e., V_{max}=240 V for the evaporated and V_{max}=200 for

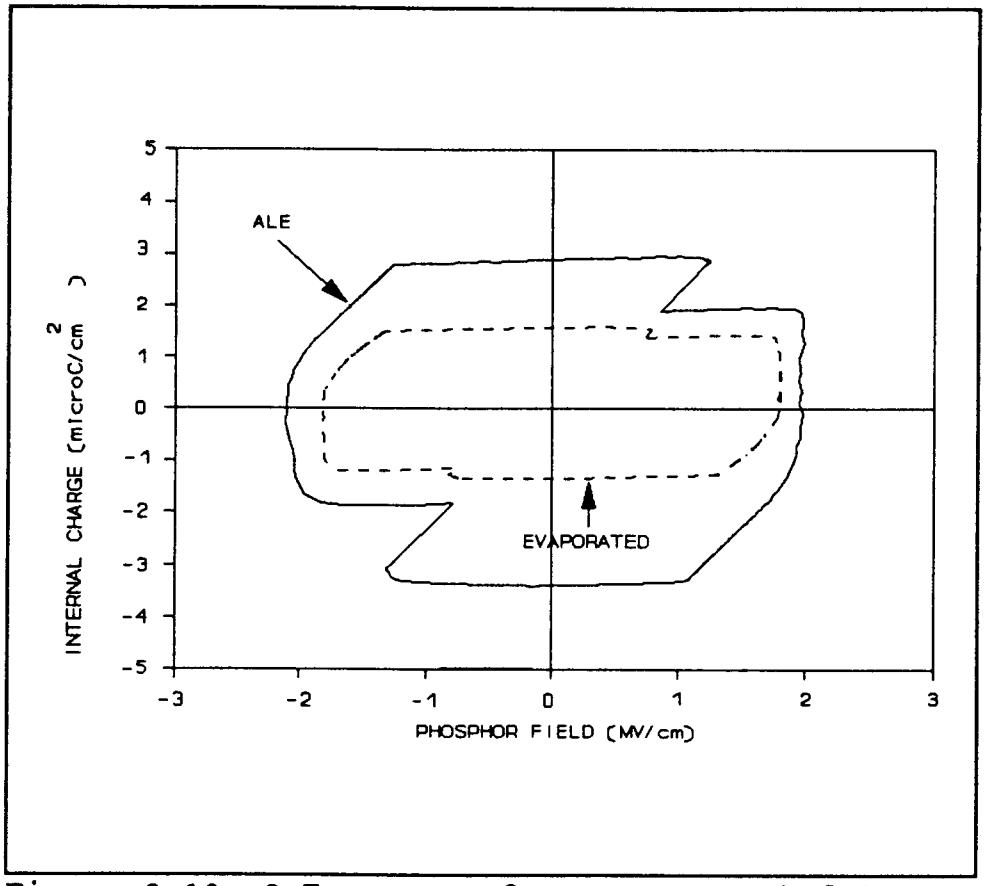

Figure 3-10: Q-F_p curves for an evaporated ZnS:Mn ACTFEL device with sputtered SiON dielectrics and for an ALE ZnS:Mn device with ATO dielectrics. Both devices are operated at approximately 60 V above threshold.

the ALE device). There are several dramatic differences between these devices. First, much more conduction charge is transported across the phosphor in the ALE device; this is a simple consequence of the larger dielectric constant of ATO (i.e., = 18.6) compared to SiON (i.e., = 6.3). Second, Q_{leak} is much more for the ALE device and the fraction of leakage to conduction charge is also much greater in the ALE device compared to the evaporated device. Thus, much of the charge transported across the ALE phosphor appears to reside in

relatively shallow traps such that it is easily emitted from

Table 3-2: A comparison of various parameters measured from the Q-F_p technique for an ALE and an evaporated ACTFEL device. + and - indicate the polarity of the voltage pulse applied to the Al electrode.

Measured parameter	ALE		Evaporated	
	+	-	+	-
F_{ss} (MV/cm)	2.1	2.0	1.7	1.7
Q_{leak} ($\mu C/cm^2$)	1.0	1.6	0.3	0.3
Q_{relax} ($\mu C/cm^2$)	2.0	2.1	1.0	1.0
Q_{cond} ($\mu C/cm^2$)	4.7	5.3	2.8	2.8
Q_{pol} ($\mu C/cm^2$)	1.9	1.8	1.3	1.3

these traps when the external bias is zeroed. Alternatively, the trap depths may be similar for the ALE and evaporated ACTFEL devices but these traps could be more readily emptied, and thus more readily contribute to the leakage charge, because of the large polarization field existing in the ALE device. Third, the evaporated ACTFEL device exhibits rather strong field-clamping. In contrast, the phosphor field in the ALE devices exhibits weak field-clamping and the magnitude and shape of the measured phosphor field depends on the polarity of the applied voltage pulse. For the ALE device, the positive

voltage pulse exhibits characteristics in which F_p increases and is constant for a very small portion of BC; the negative voltage pulse displays a larger field-clamping regime but near G a field-overshoot region exists. Finally, note that the Q-F_p characteristic is symmetric for the evaporated ACTFEL device but is rather asymmetric for ALE device.

Further comparison between the two devices is displayed by plotting a family of Q-F_p curves as a function of V_{max} in Figs. 3-11 and 3-12. Note that strong field-clamping occurs in the evaporated device whereas its absence is clearly evident in the ALE device. Also note in FIg. 3-12 near points G that

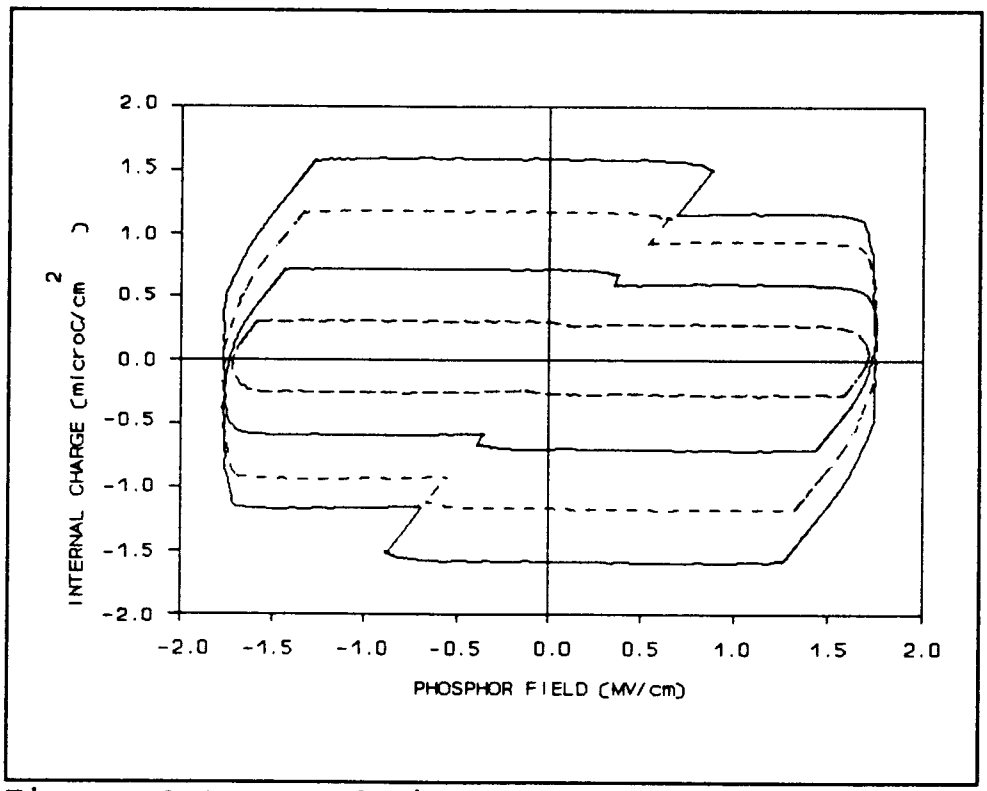

Figure 3-11: A family of Q-F_p curves for an evaporated ZnS:Mn ACTFEL device with sputtered SiON dielectrics. V_{max} = 180, 200, 220, and 240 V.

the field-overshoot region is more pronounced at larger V_{max}'s. The field-overshoot exhibited by the ALE device is

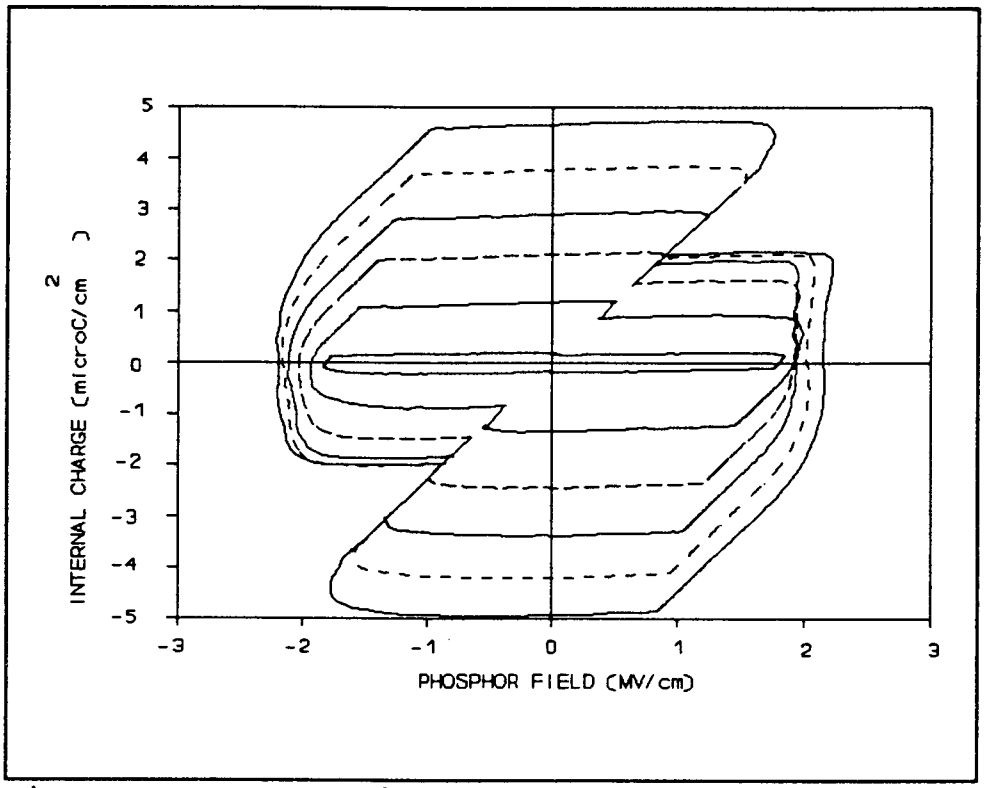

Figure 3-12: A family of Q-F_p curves for an ALE ZnS:Mn ACTFEL device with ATO dielectrics. V_{max} = 140, 160, 180, 200, 220, and 240 V.

ascribed to the existence of space charge in the phosphor bulk.[36] Field-overshoot could also arise as a consequence of a certain distribution of interface states. The field-overshoot is believed to arise from the presence of bulk space charge because the C-V overshoot is found to be concomitant with the Q-F_p overshoot. This C-V overshoot exhibits a capacitance peak well in the excess of the insulator capacitance which is inconsistent with the hypothesis that overshoot arises from interface states. Note that the

existence of bulk space charge in the phosphor invalidates Eq.(9). However, the Q-F_p technique may still be gainfully employed if it is realized that F_p calculated from Eq.(9) is actually an effective phosphor field; care must be taken in interpreting such Q-F_p curves.

3.5 SUMMARY

In this chapter, a new method, the Q-F_p technique, for electrical characterization of ACTFEL devices is introduced. This method is compared to conventional techniques used to characterize the ACTFEL devices such as Q-V and C-V analysis. The uniqueness of this technique is that the internal behavior of the ACTFEL is investigated rather than the external and internal behavior, as is the case for the Q-V technique. A combination of Q-V, C-V, and Q-F_p analysis provide a more complete electrical characterization of ACTFEL devices.

CHAPTER 4-ELECTRICAL CHARACTERIZATION OF ALE ACTFEL DEVICES SUBJECT TO VARIATIONS IN THE APPLIED VOLTAGE WAVEFORM.

4.1 INTRODUCTION

The electrical response of ZnS:Mn ACTFEL devices grown by ALE is systematically studied by varying the characteristics of the standard waveform; specifically, V_{max}, PW, and RT/FT are systematically varied. It is important to understand how the standard waveform variations effect the electrical properties of ALE devices in order to get the best performance or efficiency possible when operating flat-panel-displays. C-V and Q-F_p analysis are used to accomplish the electrical analysis. The electrical properties measured include V_{to}, Q_{pol}, Q_{leak}, F_{ss}, Q_{cond}, Q_{relax}, the phosphor field at turn-on ,F_{to}, and the interface density in the pre-clamping regime,Q_{ss}. All of these parameters are measured for both polarities of V_{max}, PW, and RT/FT.

V_{to} and Q_{ss} are measured using the C-V technique.[5,26] Q_{pol}, Q_{leak}, Q_{cond}, Q_{relax} and F_{ss} are assessed from the Q-F_p technique. F_{to} is evaluated from Q_{pol} and V_{to1} is assessed from the Q-F_p and C-V techniques, respectively.

4.2 EXPERIMENTAL RESULTS

4.2.1- V_{max} experiment

The V_{max} experiment is performed by varying the maximum applied voltage from 160 V to 240 V, where 160 V corresponds to V_{th}. PW and RT/FT are held constant at 30μs and 5μs, respectively. The experimental trends arising from a

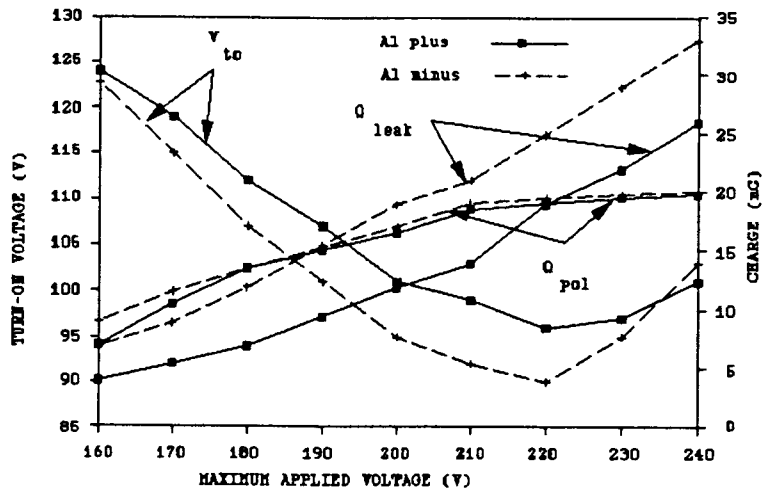

Figure 4-1: V_{to}, Q_{pol}, and Q_{leak} as a function of V_{max}.

systematic variation of V_{max} experiment are summarized in Figs. 4-1 to 4-5. As shown in Fig. 4-1, Q_{pol} increases while V_{to} decreases and then saturates while V_{to} saturates or increases. V_{to} initially decreases because of the increase in the magnitude of Q_{pol} and the concomitant increase in the polarization field in the phosphor which aids the external field, thus reducing the external voltage required to initiate tunnel emission from interface states. When Q_{pol} saturates, the magnitude of the polarization field also saturates, thus, V_{to} saturates. Further saturation in Q_{pol} requires more external field and hence an increase in V_{to}. As indicated in Fig. 4-1, Q_{leak} increases monotonically with increasing V_{max}

but with a larger slope at larger V_{max}'s. Q_{leak} increases at a distincly faster rate when Q_{pol} saturates. Thus, the amount of charge which is emitted from the interface and leaks back across the phosphor depends on the magnitude of the polarization field in the phosphor.

Figure 4-2 shows that both Q_{cond} and Q_{relax} monotonically increase with increasing V_{max}. However, the slope of the Q_{cond}-

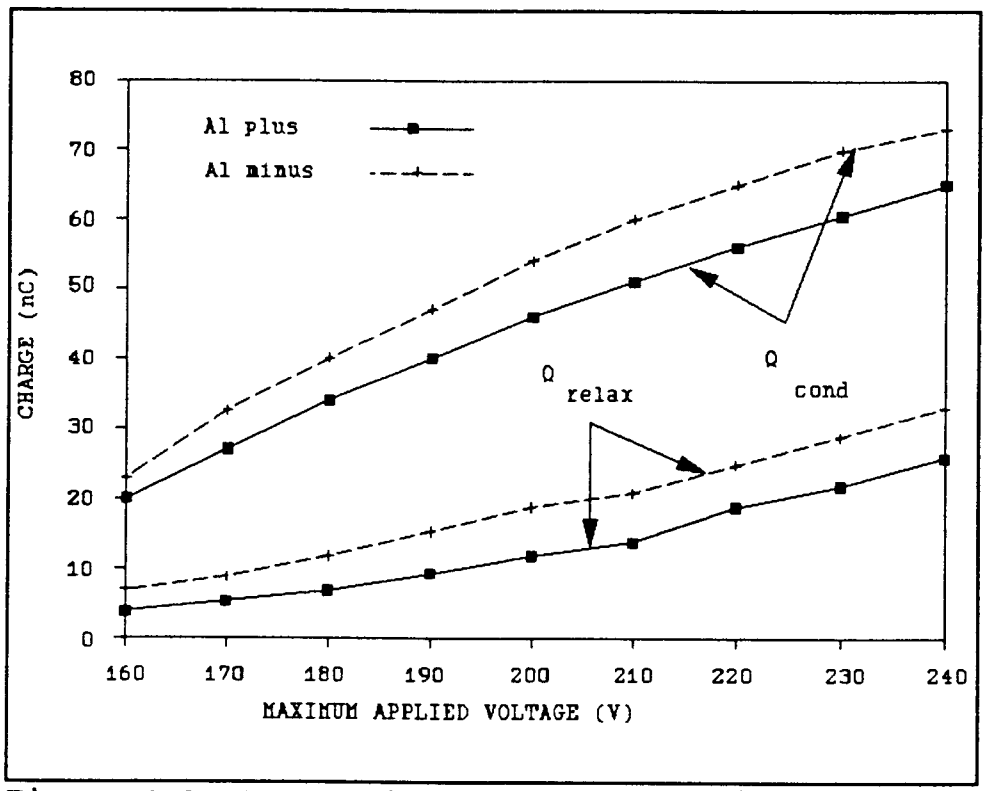

Figure 4-2: Q_{cond} and Q_{relax} as a function of V_{max}.

V_{max} curve decreases slightly at larger V_{max}'s. This decrease in slope indicates that less conduction charge is available for a given increase in V_{max}. This trend is consistent qualitatively with the saturation of Q_{pol} and the increase in

Q_{leak} observed in Fig. 4-1. Also, this trend can be understood quantitatively, with the aid of Fig. 3-4, by recognizing that

$$|Q^{\pm}_{cond}| = |Q^{+}_{pol}| + |Q^{-}_{pol}| + |Q^{\pm}_{leak}| . \tag{10}$$

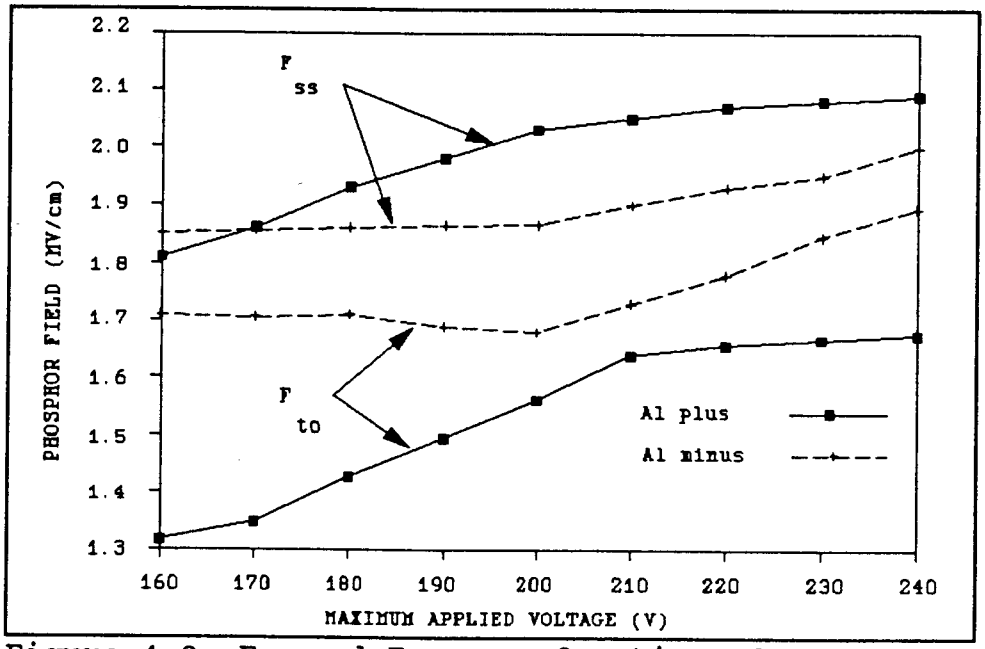

Figure 4-3: F_{ss} and F_{to} as a function of V_{max}.

Thus, if both Q_{pol}'s are constant, Q_{cond} increases as Q_{leak} increases for increasing V_{max}.

Further V_{max} trends are plotted in Figs. 4-3 and 4-4. F_{ss} and F_{to} are plotted in Fig. 4-3 versus V_{max} while Q_{ss} is plotted in Fig. 4-4 as a function of V_{max}. Figures. 4-3 and 4-4 show a very distinct voltage polarity-dependence;in contrast, the basic trends exhibited Fig. 4-1 are polarity-independent, although the actual magnitudes of the quantities do depend somewhat on the voltage polarity. The magnitude of the turn-on field, F_{to}, is established by the depth and density of the most shallow interface states while deeper interface states determine the magnitude of the steady-state

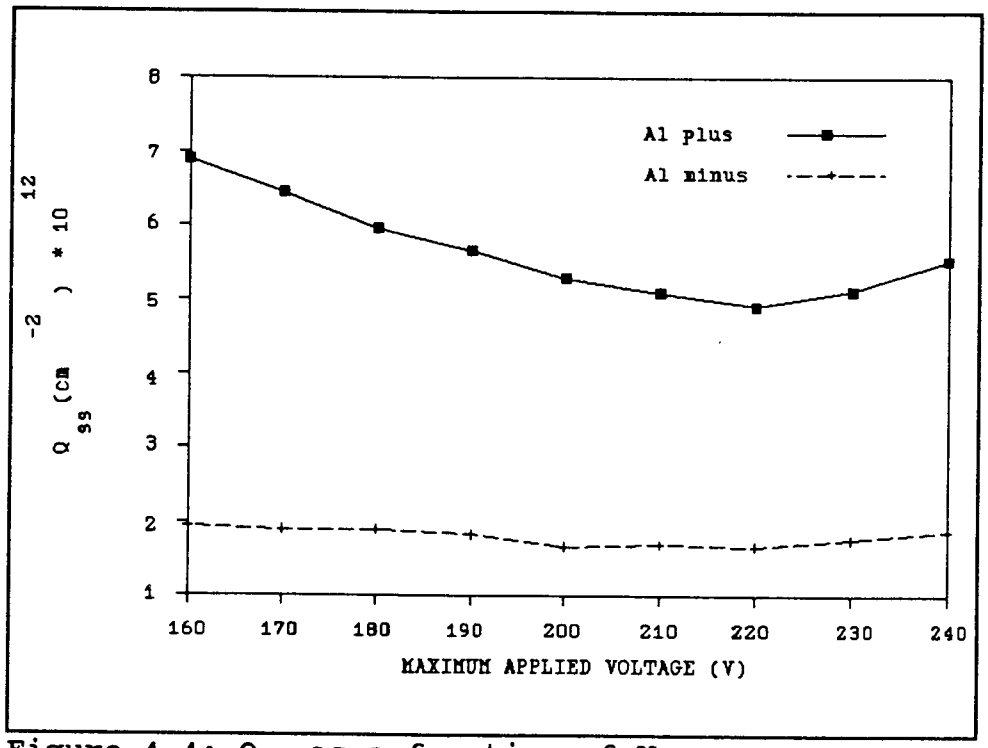

Figure 4-4: Q_{ss} as a function of V_{max}.

field, F_{ss}. F_{to} is qualitatively evaluated as follows[30]

$$|F_{to}^{\pm}| = \frac{|Q_{pol}^{\pm}| + C_i |V_{to1}^{\pm}|}{d_p (C_i + C_p)} \tag{11}$$

where the superscripts identify the appropriate polarity of the relevant quantity. It is evident that F_{to} and F_{ss} exhibit similar trends with respect to V_{max}. For V_{max} less than approximately 200 V, F_{ss}^{+} and F_{to}^{+} increase as V_{max} increases while F_{ss}^{-} and F_{to}^{-} are constant. For V_{max} greater than 200 V, F_{ss}^{+} and F_{to}^{+} saturate whereas F_{ss}^{-} and F_{to}^{-} increase with increasing V_{max}. Note that + and - correspond to the polarity of the applied voltage. The + sign corresponds to applying a positive voltage to the Al electrode while the - sign corresponds to applying a negative bias to Al electrode (see

Fig. 3-1). Complementary information is available from Fig. 4-4 which shows Q_{ss}^- to be constant while Q_{ss}^+ first decreases with increasing V_{max} until approximately 200 V and then increases for V_{max} above 200 V. Q_{ss} is evaluated from a C-V curve by measuring the slope as follows[26]

$$Q_{ss} = \frac{C_i^2 C_t}{2qAC_p}\left[\frac{\Delta C}{\Delta V}\right]^{-1} \tag{12}$$

where A is the ACTFEL device area and the quantity in the square brackets is the slope of a C-V curve.

The electrical trends shown in Figs. 4-3 and 4-4 are explained briefly as follows. The increase in F_{to}^+ and F_{ss}^+ for V_{max} less than 200 V is attributed to the fact that the ITO interface states differ from that of the Al interface in the pre-clamping regime where Q_{ss}^+ is larger than Q_{ss}^-. F_{to}^+ and F_{ss}^+ saturation for V_{max} greater than 200 V is attributed to the fact that although more charge is conducted across the phosphor at larger V_{max} (see Fig. 4-2), this additional charge leaks away from the ITO interface and does not lead to an increase in the polarization charge (see Fig. 4-1), so that the total interface charge saturates.

The fact that F_{to}^- and F_{ss}^- are constant for V_{max} less than 200 V is due to Q_{ss}^- being constant where the quasi-Fermi level does not reach clamping because of insufficient interface states. F_{to}^- and F_{ss}^- increase for V_{max} greater than 200 V is attributed to electron multiplication concomitant with build-up of space charge. The build-up of space charge is

evident in Fig. 4-5, as discussed in the following.

In summary, the trends exhibited in Fig. 4-3 are explained as follows. For V_{max} less than 200 V, F_{to}^- and F_{ss}^- are constant because of field-clamping due to the relatively large and abrupt interface state density present at the top interface while F_{to}^+ and F_{ss}^+ increase with increasing V_{max} due to a lack of field-clamping associated with a broader distribution of interface states at the bottom interface; for V_{max} greater than 200 V, F_{to}^+ and F_{ss}^+ saturate because of an exceedingly large polarization field which results in an increase in leakage charge and a saturation in the polarization charge, whereas F_{to}^- and F_{ss}^- increase with increasing V_{max} because of the build-up of space charge in the phosphor.

Figure. 4-5 shows plots of several C-V curves for a negative polarity of V_{max}. As seen in Fig. 4-5, an overshoot in the initial portion of the insulator capacitance region is apparent when the Al electrode is biased negative. This overshoot becomes more pronounced at higher V_{max}'s, specifically above 200 V. This overshoot is attributed[33] to the build-up of space charge in the phosphor layer. Also, notice that the expected C_i, calculated from the known dielectric constant and the thickness of the insulator, is 0.32 nF which is smaller than the measured C_i of the C-V curve. This is consistent with the existence of space charge. As shown in Fig. 4-6, the C_i measured when the Al is biased

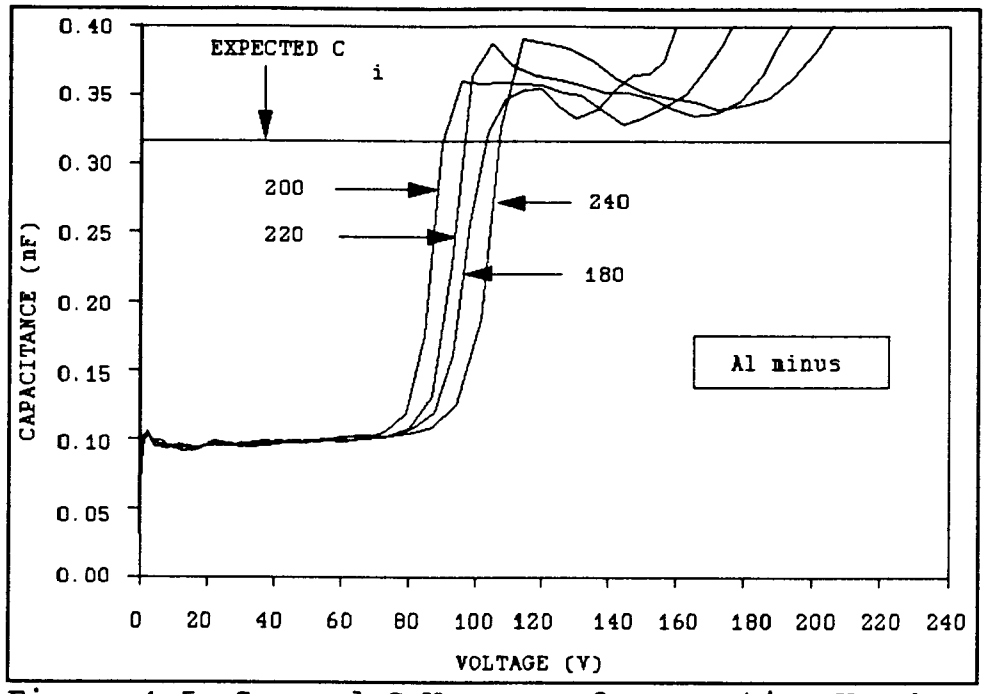

Figure 4-5: Several C-V curves for negative V_{max}'s.

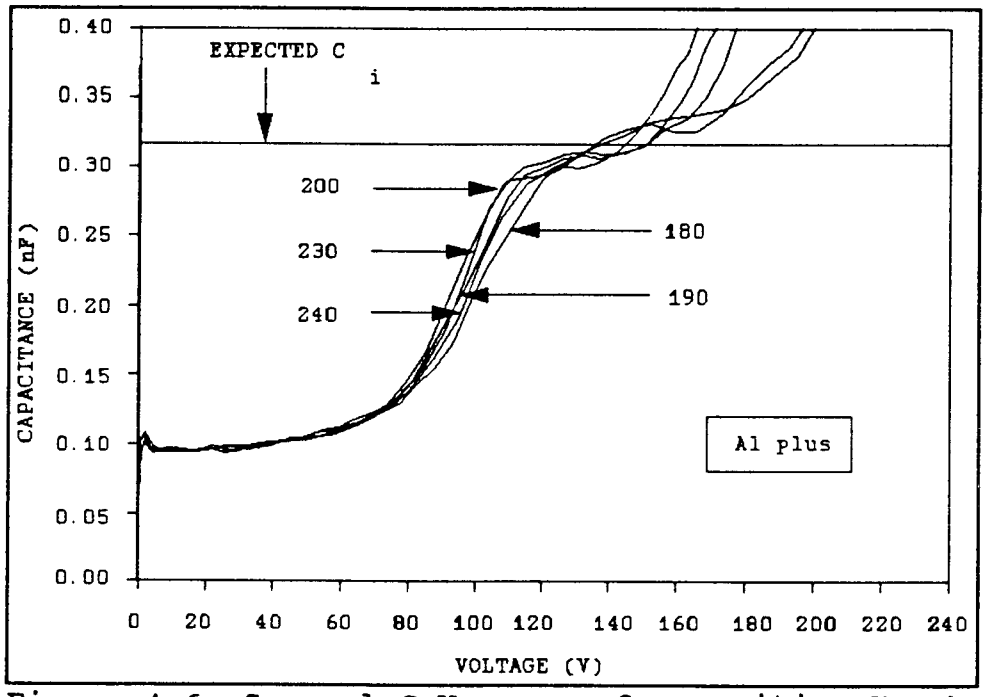

Figure 4-6: Several C-V curves for positive V_{max}'s.

positive is in closer agreement with the expected C_i. The origin of space charge is believed[33] to be associated with

impact ionization of zinc vacancies, given rise to a region of positive space charge located near the anode (i.e., ITO) interface. The zinc vacancies are thought to be located near the ITO interface. Impact ionization of these zinc vacancies reduces the average phosphor field slightly and reduces the phosphor field near the anode interface significantly.

4.2.2- PW experiment

The PW experiment is performed by varying the pulse width of the driving waveform from 3μs to 37μs while V_{max} and RT/FT are fixed at 200 V and 5μs, respectively. The experimental trends arising the from PW experiment are summarized in Figs. 4-7 to 4-10. The electrical trends resulting from variation of PW are similar to the electrical trends arising from the variation of V_{max} experiment but with a lesser degree of dependence. As shown in Fig. 4-7, Q_{pol} increases and then saturates while V_{to} decreases and then saturates. Q_{leak} increases and saturates. The fact that Q_{pol} increases while V_{to} decreases is due to the increase in the polarization field established in the phosphor which reduces the external field needed to initiate emission from interface states and hence reduces V_{to}. When Q_{pol} saturates, V_{to} saturates because the polarization field saturates. The Q_{leak} trend is explained by referring to Fig. 4-8 in which Q_{cond} increases and then saturates in the same manner as Q_{leak}. This is explained as in the V_{max} experiment; i.e. the saturation in Q_{cond} is consistent with the saturation of Q_{pol} and Q_{leak}, (see Eqn. (10)). Q_{relax}

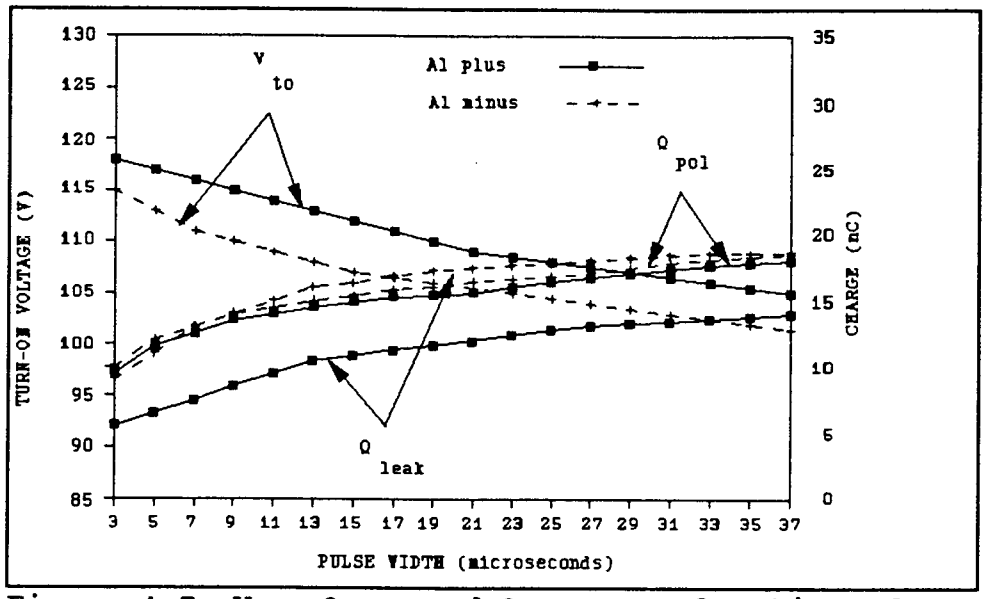

Figure 4-7: V_{to}, Q_{pol}, and Q_{leak} as a function of PW.

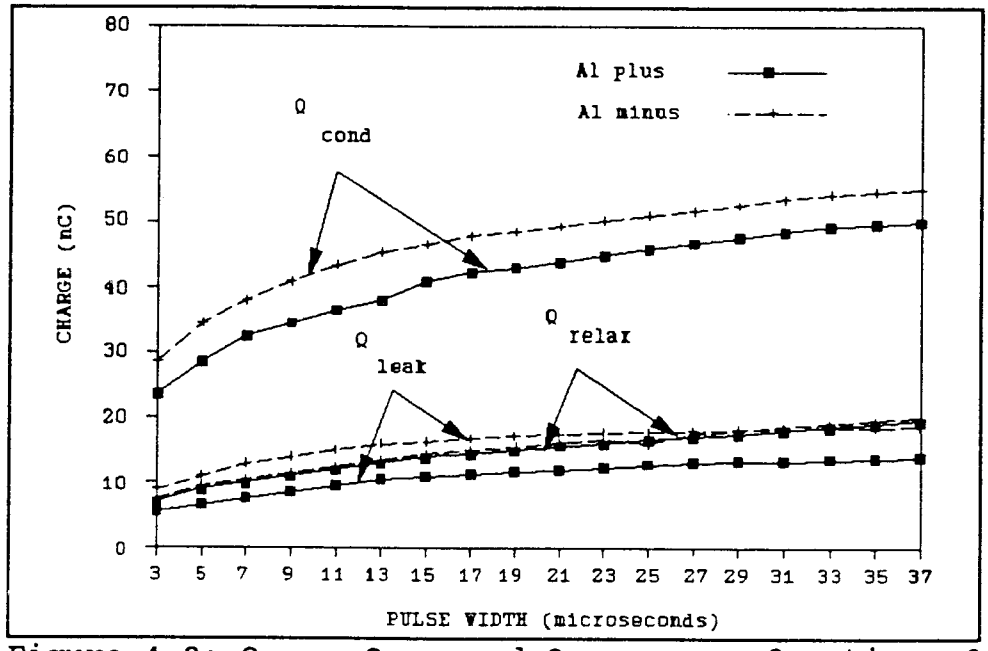

Figure 4-8: Q_{leak}, Q_{cond} and Q_{relax} as a function of PW.

also increases with increasing PW but with a lesser slope at larger PW. The modulation of this charge gives rise to the PW dependence observed in Figs. 4-7 and 4-8.

Further PW trends are plotted in Figs. 4-10 and 4-11. As

shown in Fig. 4-9, Q_{ss} is relatively insensitive to PW

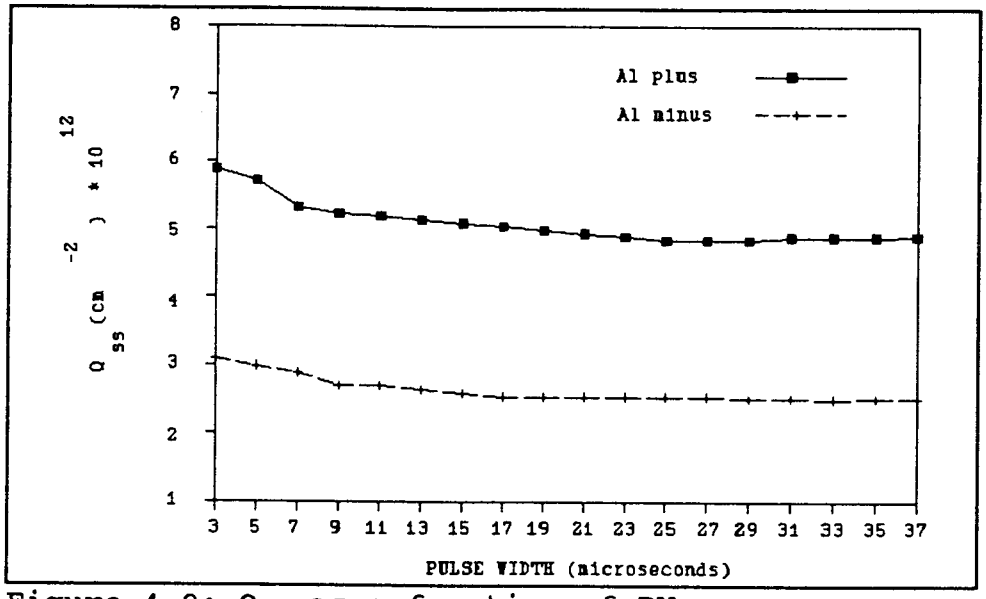

Figure 4-9: Q_{ss} as a function of PW.

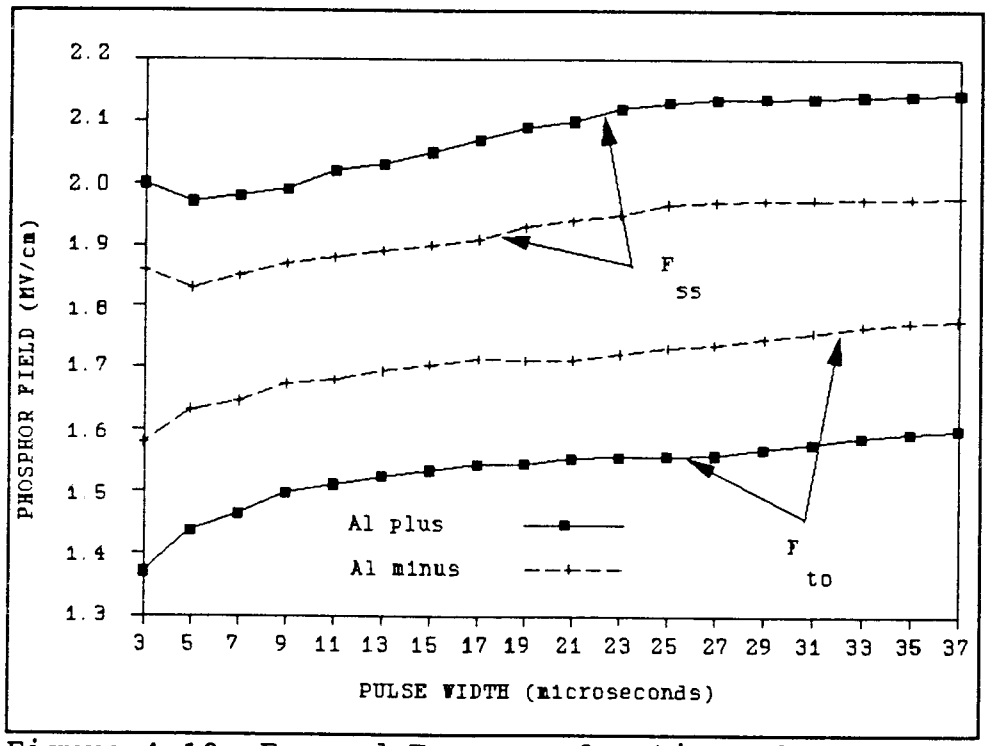

Figure 4-10: F_{ss} and F_{to} as a function of PW.

variartions. The general trend in Fig. 4-10 is for F_{ss} and F_{to}

to increase and then saturate with increasing PW. This trend is a simple consequence of the corresponding increase in Q_{pol} and the polarization phosphor field. Note that F_{to} and Q_{ss} have the greatest amount of polarity dependence of all the quantities plotted in Figs. 4-9 to 4-10; this underscores that it is primarly a difference in the interface state density of the two interfaces which is responsible for the polarity-dependent properties of ALE ZnS:Mn ACTFEL devices.

4.2.3 RT/FT experiment

The RT/FT experiment is performed by varying the rise and fall time from 1μs to 19μs while V_{max} and PW are held constant at 200 V and 30 μs, respectively. The main experimental results arising from this experiment are summarized in Figs. 4-11 to 4-14. As seen in these figures, the electrical

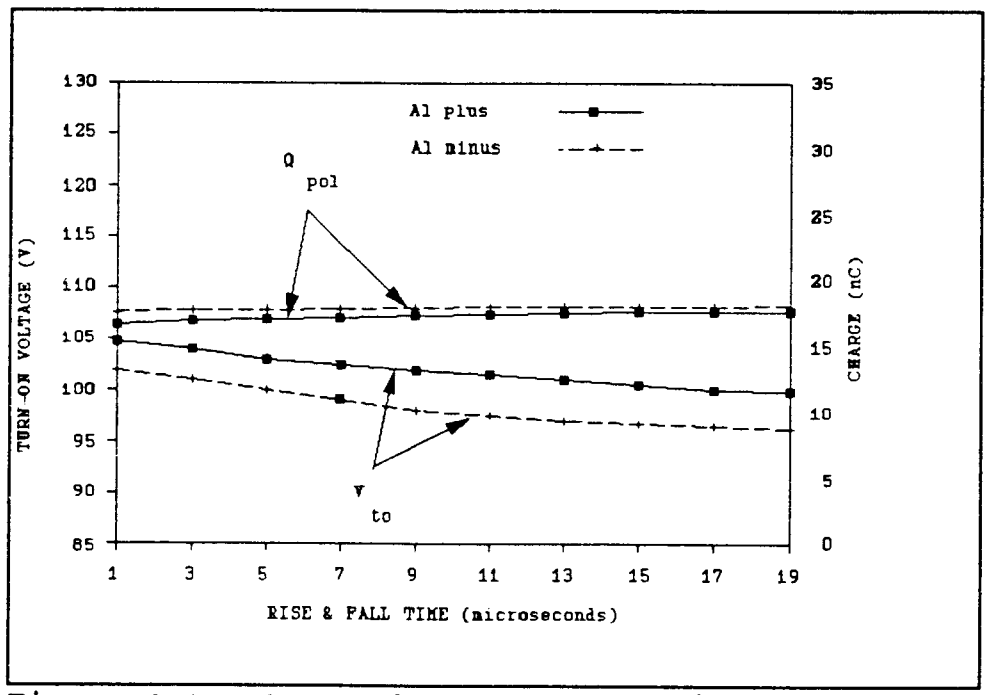

Figure 4-11: Q_{pol} and V_{to} as a function of RT/FT.

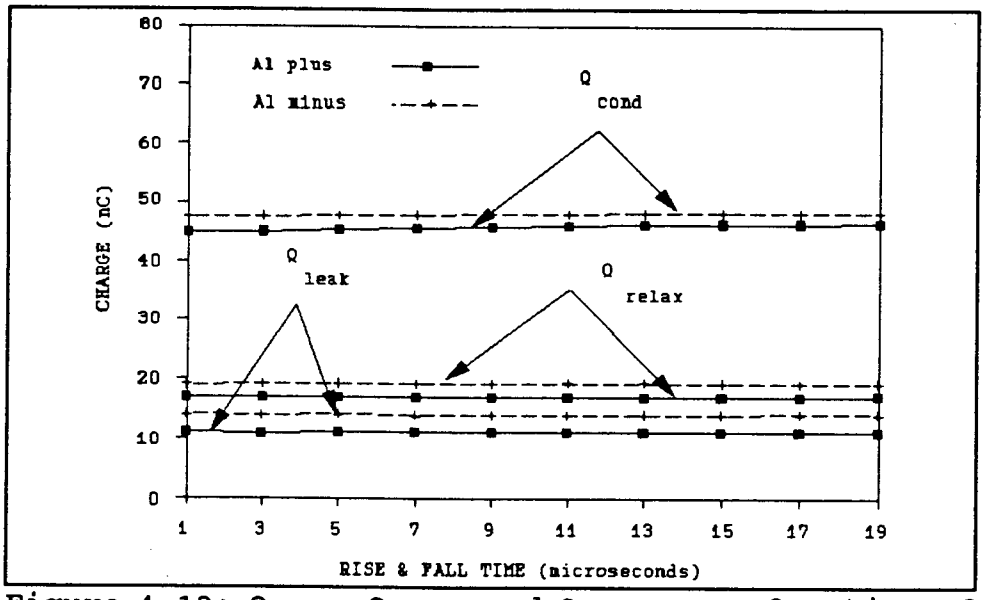

Figure 4-12: Q_{leak}, Q_{cond}, and Q_{relax} as a function of RT/FT.

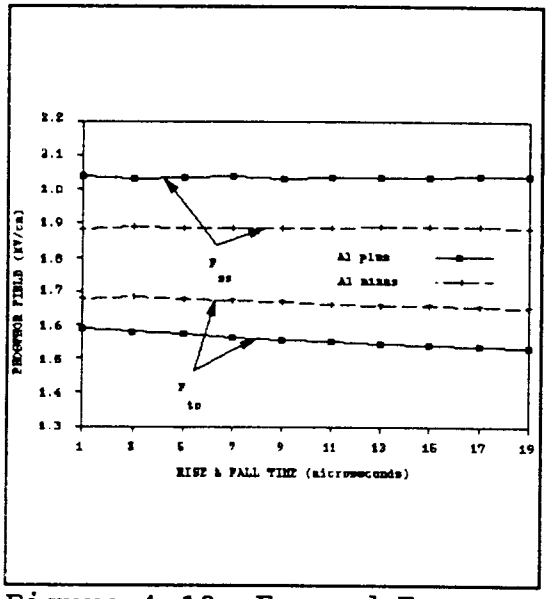

Figure 4-13: F_{ss} and F_{to} as a function of RT/FT.

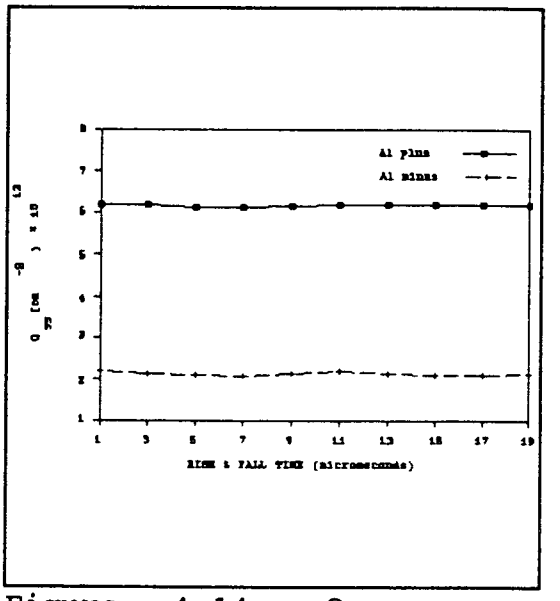

Figure 4-14: Q_{ss} as a function of RT/FT.

properties are relatively independent of RT/FT. This is expected since the rise and fall times of the applied voltage are not expected to initiate more charge from interface states or modulate the time in which the charge relaxes.

4.3 **Summary**

Varying V_{max}, PW, and RT/FT of the driving waveform show that V_{max} has the strongest effect of all, PW has an itermediate effect, and the RT/FT has almost no effecet on the electrical properties of ZnS:Mn ACTFEL devices grown by ALE. ALE devices are found to exhibit a polarity-dependent asymmetry attributed primarily to an asymmetry of the interface state density and to the presence of space charge in the phosphor layer. The results herein should assist in efforts to model ALE ZnS:Mn ACTFEL devices.

CHAPTER 5 - ACTFEL AGING STUDIES

5.1 INTRODUCTION

Device stability and aging studies of ACTFEL devices are of fundamental importance to the ACTFEL industry. The device stability from the electrical point of view, is controlled, to a certain extent, by the process method used to fabricate the ACTFEL device. For example, ZnS:Mn ACTFEL devices fabricated by evaporation[30] exhibit different aging mechanisms than devices grown by ALE.[10]

In this chapter, a short-term aging study of ZnS:Mn ACTFEL devices grown by ALE is presented in order to establish the nature and kinetics of aging and to determine the aging mechanism. The electrical properties are measured as a function of aging time at room temperature for both polarities. Based on measured parameters such as V_{to}, F_{ss}, F_{to}, Q_{cond}, Q_{pol}, Q_{leak}, and Q_{ss}, a discussion of a possible aging mechanism for ALE ZnS:Mn ACTFEL devices is presented. Furthermore, solutions for improving the stability of ALE ZnS:Mn ACTFEL devices are introduced.

5.2 EXPERIMENTAL DESCRIPTION

The aging experiment is undertaken by monitoring the Q-F_p and C-V characteristics as a function of time. C-V and Q-F_p characteristics are described in sections 3.2 and 3.3, respectively. Aging of the ACTFEL devices is conducted at room temperature. The longest aging time employed was 50 hours. All of the electrical characterization is accomplished in an

automated fashion such that the aging is carried out under continuous applied field. The driving waveform used in this experiment is the standard waveform described earlier in section 2.2 with a voltage amplitude of 210 V. The aging is also performed on a single glass sample provided by Planar International. The sample contains 10 aluminum dots, each has an area of 0.0104 cm^2. The system set-up is shown in Fig. 3-1 in section 3.2.

5.3 AGING RESULTS

The results of ACTFEL aging experiments using glass number 9-6-91-DSD1 are presented as follows. Figure 5-1

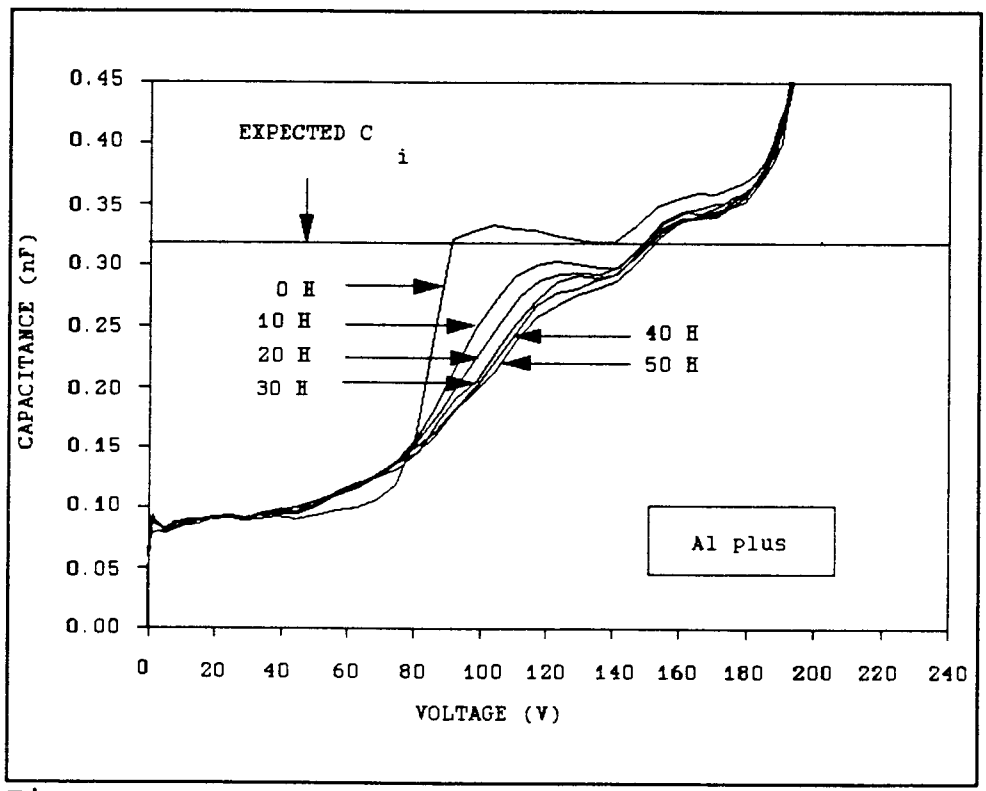

Figure 5-1: C-V curves as a function of aging time for an ALE ACTFEL device when the Al electrode is biased positive.

illustrates the C-V characteristics as a function of aging time for a positive voltage pulse applied to the Al electrode (i.e., electrons are emitted from the ITO interface). Note that the C-V curve shifts in a non-rigid manner with respect to aging time; this non-rigid shift in the C-V curve indicates that the interface state density in the pre-clamping regime,[26] Q_{ss}, increases as a function of aging time, as displayed quanitatativelly later. Moreover, notice how soft the C-V curve becomes in the V_{to1} regime as aging continues; this softening indicates that electrons are injected from shallower interface states as aging progresses. Finally, note that C_i decreases with aging time; most of the decrease in C_i occurs

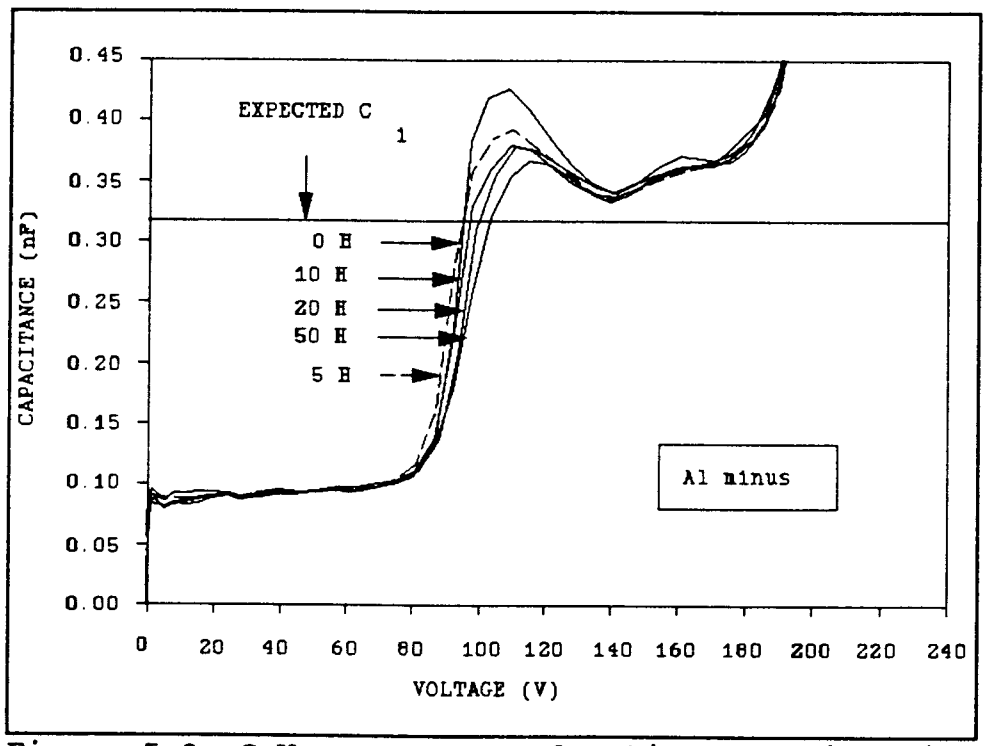

Figure 5-2: C-V curves as a function of aging time for an ALE ACTFEL device when Al electrode is biased negative.

during the initial 10 hours of aging.

Figure 5-2 shows C-V curves corresponding to various aging times for a negative voltage pulse applied to the Al electrode (i.e., electrons are emitted from the Al interface). It is evident from a comparison of Figs. 5-1 and 5-2 that the C-V curves corresponding to the two interfaces are quite different initially and that they display distinctly different aging trends. Hence, the electrical properties and aging characteristics of these interfaces are also quite different. The asymmetry trends observed by C-V analysis are very similar to the conduction current-voltage curves reported[31] by Mikami et al. Perhaps the most unusual aspect of the curves shown in Fig. 5-2 is the overshoot which is interpreted[7,9] as evidence for the build-up of space charge in the bulk ZnS phosphor. An overshoot in the Q-F_p characteristics is also observed concomitant with C-V overshoot; this is further evidence for space charge.[7,9] Notice that the extent of the overshoot decreases with aging. Figure 5-3 shows this overshoot as a function of aging time. As seen, the overshoot decreases by about 13% for 50 hours of time. Therefore, the amount of space charge build-up in the ZnS decreases by approximately the same amount with aging time.

The second trend evident from Fig. 5-2 is that the C-V curve first shifts rigidly to lower voltages and then shifts almost rigidly to higher voltages with increasing aging time. This rigid or almost rigid shift is interpreted[5,26] as

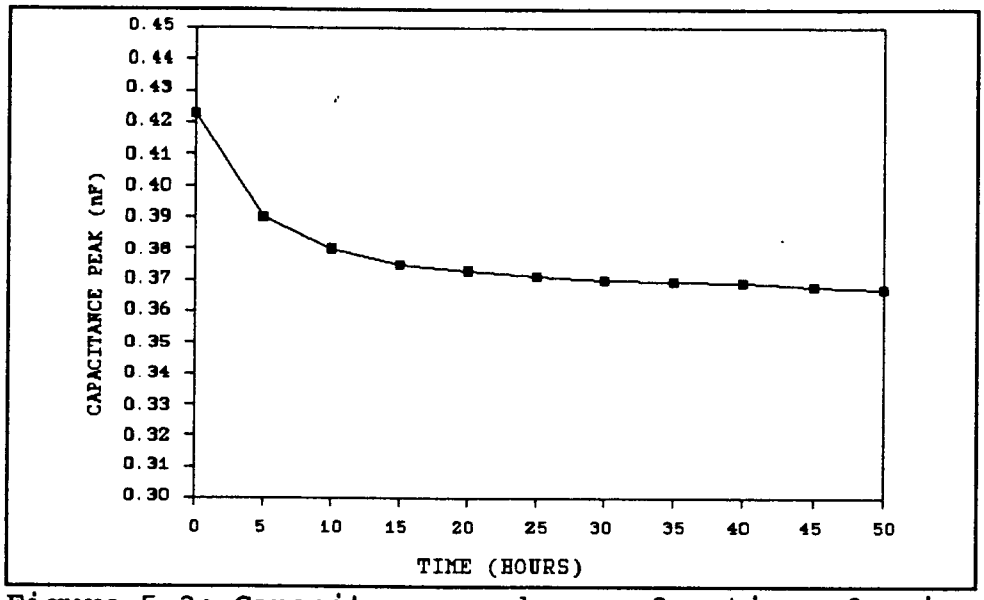

Figure 5-3: Capacitance peak as a function of aging time.

indicating that Q_{ss} is rather constant with aging. Furthermore, since these C-V curves are rather steep, Q_{ss} is relatively small.[5,26]

Several of the C-V trends discussed previously are summarized in Figs. 5-4 and 5-5. Figure 5-4 is a plot of V_{to2} as a function of aging time. V_{to2} for the ITO electrode (i.e., Al plus) monotonically increases with aging time as the C-V transition becomes broader. V_{to2} for the Al electrode (i.e., Al minus) first decreases, then increases, and finally saturates at a voltage similar to its original value. Figure 5-5 indicates the dramatic difference in the Q_{ss} aging trends for the two interfaces. Both interfaces exhibit an increase in Q_{ss} with aging time, but the change in the ITO interface is much larger.

Various other aging trends are shown in Figs. 5-6 and 5-

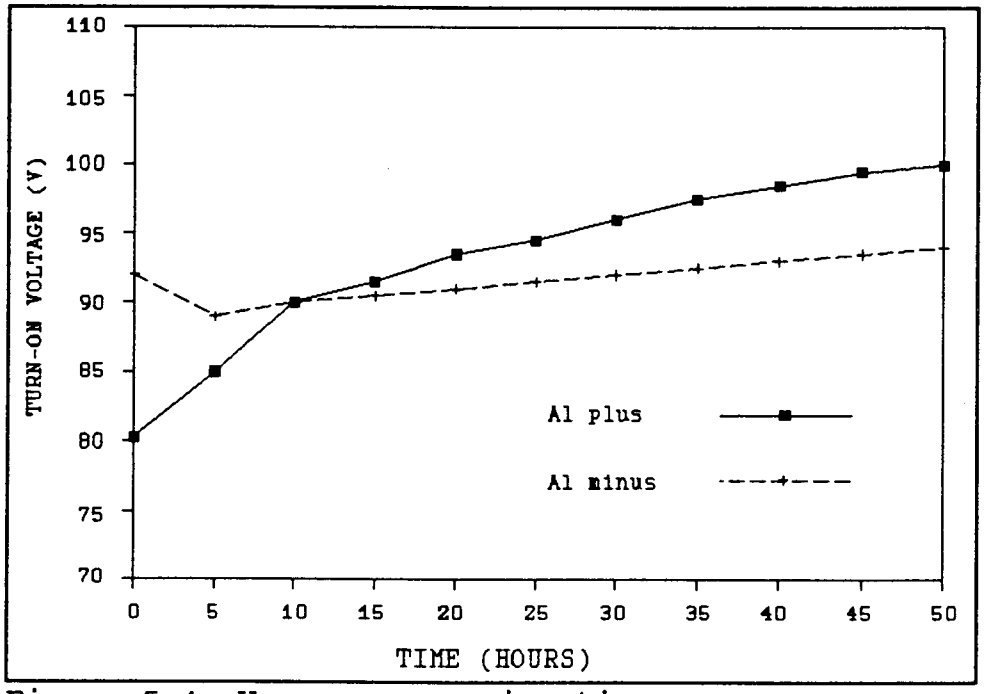

Figure 5-4: V_{to2} versus aging time.

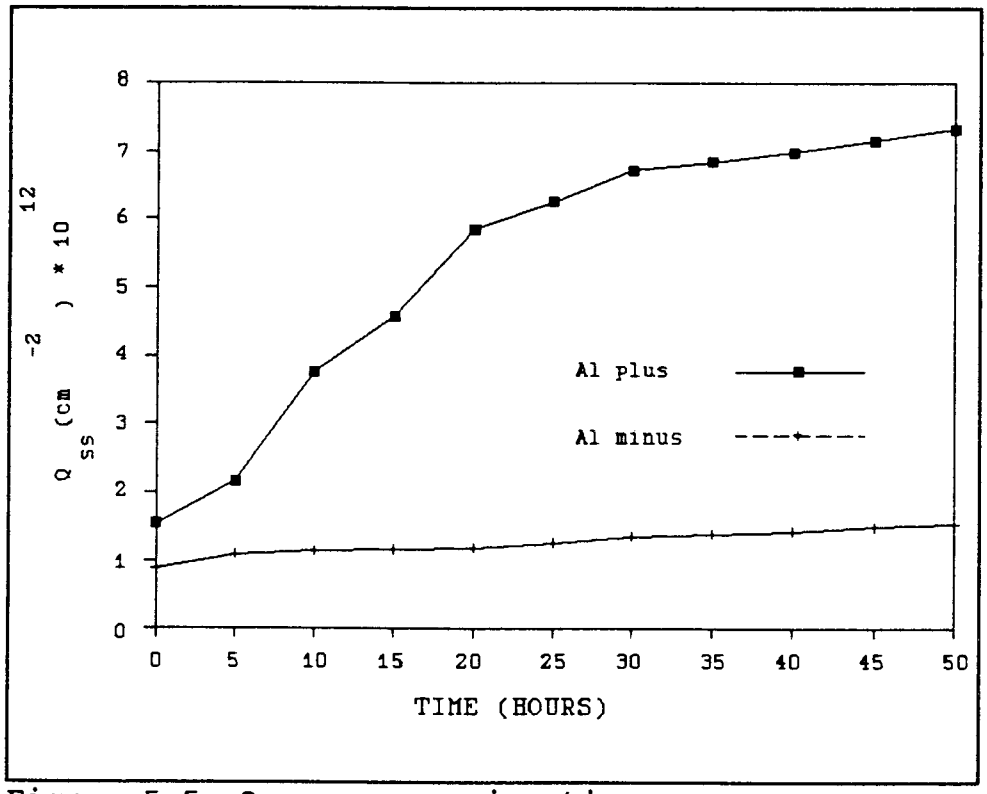

Figure 5-5: Q_{ss} versus aging time.

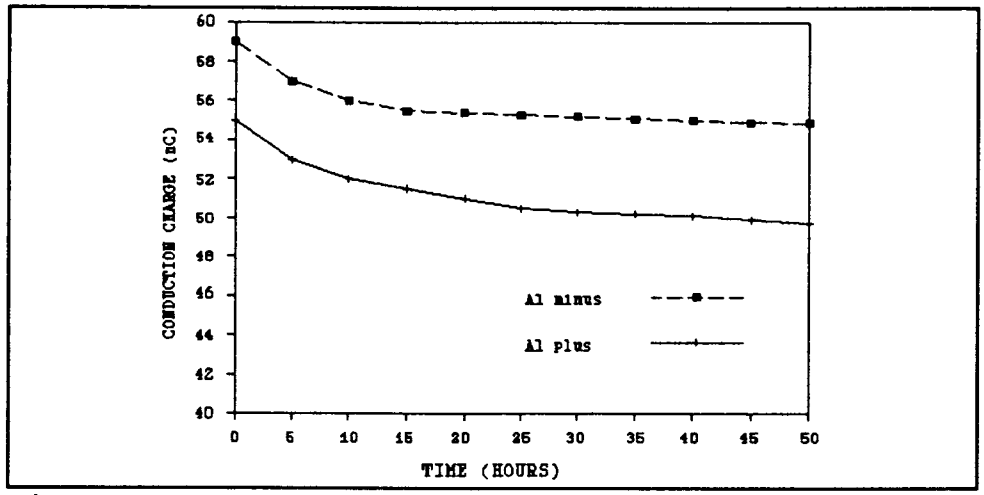

Figure 5-6: Q_{cond} versus aging time.

Q_{cond} is plotted as a function of aging time in Fig. 5-6. As seen in Fig. 5-6, Q_{cond} decreases with aging time but this decrease nearly saturates at long aging time. Q_{pol} and Q_{leak} are plotted in Fig. 5-7. It is evident from Fig. 5-7 that Q_{leak}

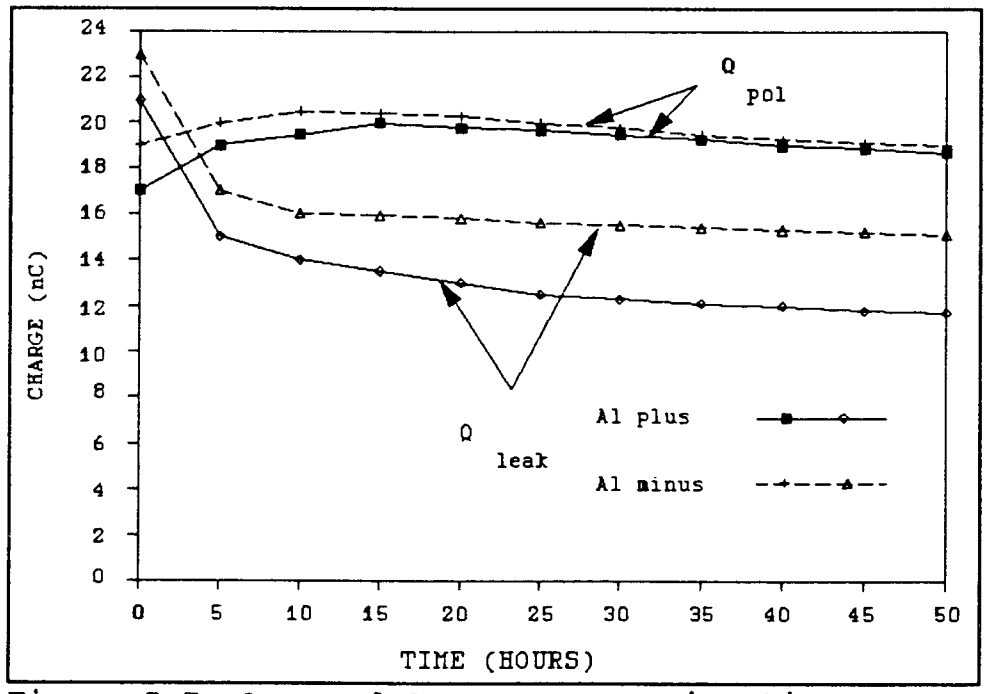

Figure 5-7: Q_{pol} and Q_{leak} versus aging time.

decreases and nearly saturates in nearly the same manner as

Q_{cond}. The striking similarity between the Q_{cond} and Q_{leak} aging trends, together with the fact that Q_{pol} is almost constant with aging time, implies that any change in Q_{cond} actually arises from a concomitant change in Q_{leak}. The observed decrease in Q_{leak} is attributed to the creation of deep interface states, as discussed later. Note that for evaporated ZnS:Mn ACTFEL devices, Q_{pol} decreases and saturates with aging time,[30] in contrast to that observed in Fig. 5-7 in which Q_{pol} is approximately constant.

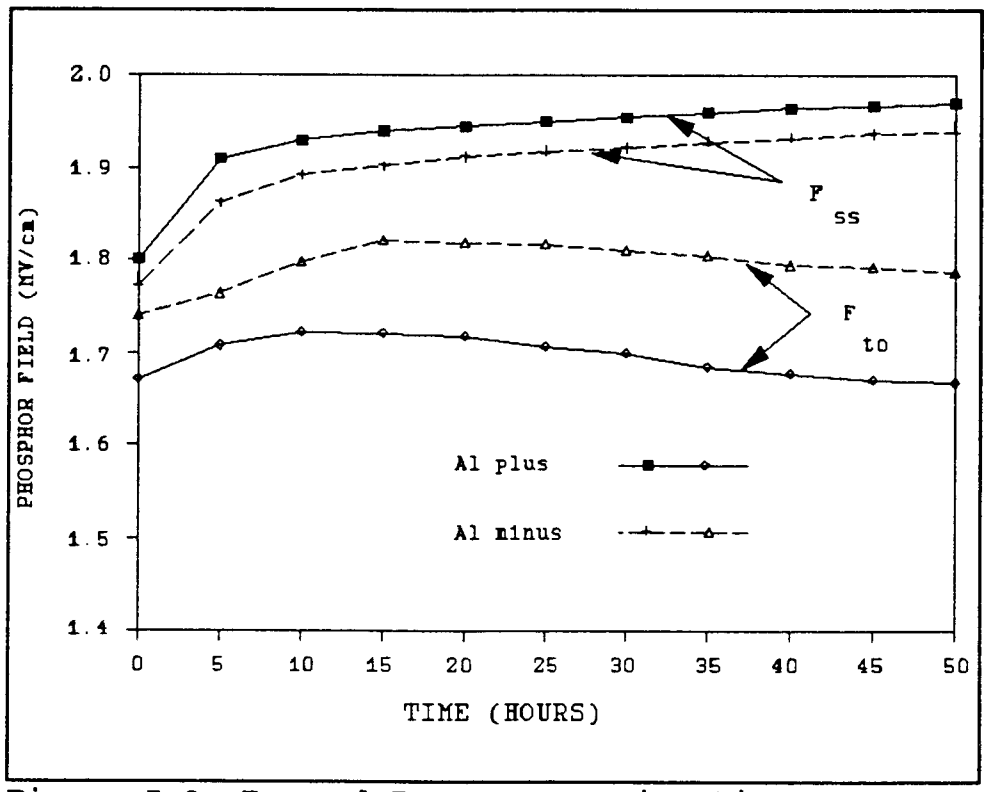

Figure 5-8: F_{ss} and F_{to} versus aging time.

F_{ss} and F_{to} are plotted for both polarities as a function of aging time in Fig. 5-8. As shown in Fig. 5-8, F_{ss} first increases with aging time and then saturates for both

polarities. In contrast, F_{to} initially increases slightly but then decreases a bit and finally saturates.

The effective insulator capacitance, C_i, is plotted as a function of aging time in Fig. 5-9. C_i is evaluated from the Q-F_p fitting procedure described in section 3.3 for a negative bias applied to the Al electrode and from C-V analysis for a positive bias applied to the Al electrode. There is good agreement between C_i as assessed from the C-V and Q-F_p techniques for the case of a positive bias applied to the Al electrode.

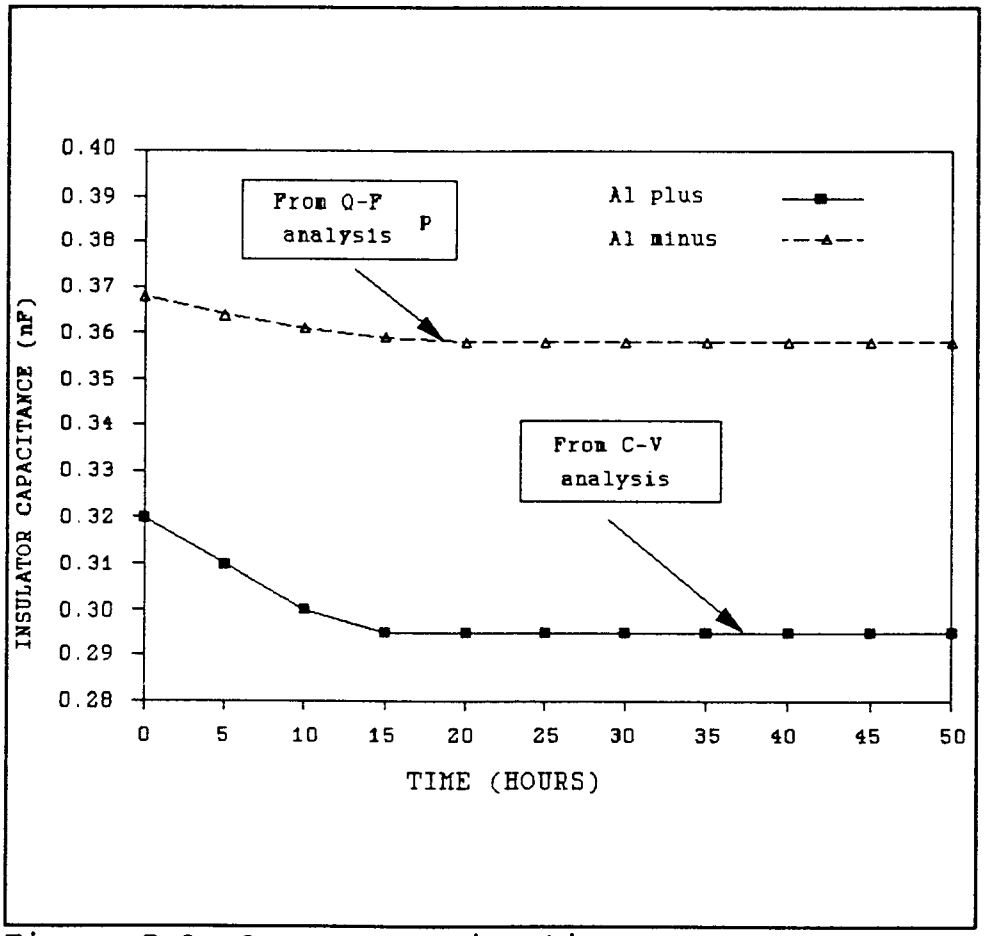

Figure 5-9: C_i versus aging time.

5.4 DISCUSSION

5.4.1 EXPERIMENTAL TRENDS

The most striking implication of the aging trends is that the interface state distributions at the Al and ITO interfaces are asymmetric and, furthermore, exhibit highly asymmetric aging characteristics. This trend is clearly illustrated by the Q_{ss} aging trends shown in Fig. 5-5. Other evidence that the interface state densities are asymmetric is implicit in Fig. 5-8 since the magnitude of F_{to} is indicative of the relative depth of the most shallow, filled interface states whereas the magnitude of F_{ss} is related to the energy depth of electrons emitted from deeper interface states. Additionally, the Q_{cond} aging trends shown in Fig. 5-6, to changes in the interface state density. Q_{cond} decreases with aging time and most of this decrease occurs in the first 10-20 hours of aging. This decrease in Q_{cond} is a direct consequence of the concomitant decrease in Q_{leak} shown in Fig. 5-7. These trends are ascribed to the creation of deeper interface states during the initial portion of the aging; an atomic mechanism for the creation of deep interface states is proposed below.

Recall from Fig. 5-1 that the effective insulator capacitance, C_i, decreases as a function of aging and most of this decrease occurs during the first 10 hours of aging. A decrease in C_i is also present in Fig. 5-2, but it is obscured by the C-V overshoot due to the space charge in the phosphor. The change in C_i is plotted in Fig. 5-9. The change in the

effective insulator thickness associated with a change in the insulator capacitance from 0.32 initially to 0.29 nF at an aging time of 50 hours corresponds to a thickness of approximately 500 angstroms. Thus, the centroid of charge near the phosphor/insulator interface changes by the order of 500 angstroms during 50 hours of aging. Since C_i decreases, d_i must increase with aging time. Hence, the effective insulator thickness increases with aging time which means that the electrode charge is balanced by a charge distribution whose charge centroid is deeper into the phosphor than before aging. Although this estimation of the change in d_i as 500 angstrom is rather crude, the important points are that the charge centriod changes quite markedly and that it moves further into the phophor.

Figure 5-2 shows a dramatic softening of the turn-on characteristics in the V_{to1} region. This is attributed to the creation of shallow states. Although these states could be interface states, they are ascribed to the creation of bulk states, as discussed below.

In summary, an assessment of the experimental data shown in Figs. 5-2 through 5-10 leads to the following conclusions regarding the aging characterstics of ALE ZnS:Mn ACTFEL devices:

(1) The interface state densities of the top and bottom interface are distinctly different and exhibit different aging characteristics.

(2) Both shallow and deep traps are created during aging at the bottom interface.

(3) A lesser number of predominately deep traps are created at the top interface during aging.

(4) The decrease in C_i with aging indicates that some of the "interface state charge" actually moves deeper into the ZnS bulk with aging.

(5) The decrease in the C-V overshoot of the bottom interface indicates that the amount of space charge build-up in the ZnS decreases with aging time.

5.4.2 AN AGING MODEL FOR ALE ZnS:Mn ACTFEL DEVICES

The experimentally established aging trends are interpreted in terms of the following model. The asymmetry in the interface state density is attributed to the presence of Cl atoms near the bottom interface; Cl is presumed to be present in significantly lower concentrations at the Al interface. Chlorine on a sulfur site, Cl_s, is known to be a relatively shallow donor in bulk ZnS. It is likely that Cl at the interface gives rise to shallow interface states. Note that Thioulouse et al. previously have attributed shallow interface states at the bottom interface to the presence of Cl in their evaporated ZnS ACTFEL devices doped with $MnCl_2$.[34]

The creation of shallow states at the bottom interface and the movement of the charge centriod into the ZnS bulk concomitant with the decrease in C_i is associated with aging-induced migration of Cl away from the ITO interface into the

ZnS bulk with aging time. Cl diffuses quickly in II-VI compounds.[35] Additionally, as Cl migrates away from the bottom interface and deeper into the ZnS, sulfur vacancies, V_s's, are left behind at the interface. The creation of deeper interface states at the bottom interface is ascribed to the formation of V_s's. Various researchers previously have concluded that V_s's are the source of interface states in ZnS ACTFEL devices.

Additionally, the migration of Cl away from the bottom interface with aging is believed to be responsible for the experimentally observed reduction in the build-up of space charge in the ZnS. Previously, an atomic model for the build-up of space charge in ALE ZnS:Mn ACTFEL devices has been proposed[33] in which zinc vacancies, V_{zn}'s, present in the Zn near the bottom interface are impact ionized by electrons injected from the top interface transiting the ZnS. Annihilation of these V_{zn}'s is one possible way in which the extent of the build-up of space charge could be reduced. However, it is difficult to correlate V_{zn}'s annihilation with Cl migration since Cl presumably would move exclusively on the S sublattice. Also, it is highly unlikely that V_{zn}'s in the ZnS bulk could be annihilated by a nearest-neighbor hopping process because of the energetics of forming an antisite defect in a II-VI semiconductor. Rather than a reduction in the V_{zn} concentration, it is proposed that the observed decrease in the build-up of space charge with aging is the result of a reduction in the local electric field near the

bottom interface, where the V_{zn}'s are localized, due to the migration of Cl. Thus, transiting electrons near the bottom interface are no longer sufficiently energetic to impact ionize V_{zn}'s; this leads to a reduction in the amount of build-up of space charge as aging proceeds.

Aging trends of the top interface are attributed to the creation of deeper interface states with aging. Most of the Cl is believed to reside at or near the bottom interface. Therefore, Cl migration can not account for the aging trends exhibited by the top interface. It is more likely that hot electron-induced atomic rearrangement at the interface gives rise to the creation of deeper interface states. It is tempting to postulate that hot electron impingement and recombination at the top interface dislodges sulfur atoms, thus creating V_s's which constitute the deep interface states that account for the observed increase in Q_{ss}, F_{to}, and F_{ss} and the decrease in Q_{cond} and Q_{leak} with aging time. Although this is currently a best guess as to what occurs at the top interface with aging, the existent data does not unequivocally support the uniqueness of this postulates.

5.5 CONCLUSIONS

An experimental study of the aging characteristics of ALE ZnS:Mn ACTFEL devices is presented in which aging is assessed by monitoring the electrical properties of these devices via C-V and Q-F_p analysis. The electrical properties of these ALE devices are asymmetrical with respect to the polarity of the

applied voltage pulse. This behavior is in contrast to the evaported ZnS:Mn ACTFEL devices whose electrical and optical properties are quite symmetric.[30] This asymmetry is in good agreement, however, with the results of previous workers.[31,34] The experimentally observed asymmetry of the electrical properties is attributed to be a consequence of differences in the interface state densities of top and bottom interfaces. Moreover, these interface state differences are believed to be due to the preferential presence of Cl at or near the bottom interface. This Cl migrates away from the bottom interface with aging and into the ZnS bulk leaving behind V_s's which are the source of deep interface states during aging. The reduction in the build-up of space charge with aging is caused by migration of Cl away from the bottom interface into the ZnS bulk; Cl_s is donor in ZnS and these donors reduce the field in the ZnS near the bottom interface, thus precluding impact ionization of V_{zn}'s and, hence, the build-up of space charge.

CHAPTER 6-CONCLUSIONS AND RECOMMENDATIONS FOR FUTURE WORK

The main achievements of this thesis are the development of the Q-F_p technique, electrical characterization of ALE ZnS:Mn ACTFEL devices subject to variations in the applied voltage waveform, and an aging study of ALE ZnS:Mn ACTFEL devices. The Q-F_p analysis is unique in the sense that it exclusively characterizes the internal behavior of an ACTFEL device. A combination of Q-F_p and C-V analysis provides a more complete picture of the internal device physics operation of an ACTFEL device. The Q-Fp technique is employed for aging studies by monitoring the internal electrical properties of ACTFEL devices such as Q_{pol}, Q_{leak}, Q_{relax}, Q_{cond}, and F_{ss} as a function of aging time.

Q-F_p and C-V analysis are first used to electrically characterize ALE ZnS:Mn ACTFEL devices subject to various applied voltage waveforms. From this experiment, the following observations can be made:

1) V_{max} variation has the strongest effect on the electrical properties of ACTFEL devices while PW variation has an intermediate effect and RT/FT has the least effect.
2) The electrical response of ALE ZnS:Mn ACTFEL devices is found to be asymmetric with respect to the polarity of the applied voltage pulse; this asymmetry is attributed mainly to an asymmetry of the interface

state density but also to the presence of space charge in the phosphor layer.

3) An overshoot in the C-V and Q-F_p curves provides evidence for the existence of space charge in the ZnS layer. The origin of this space charge is believed to be associated with impact ionization of zinc vacancies, giving rise to a region of positive space charge located near the bottom interface.[33] Impact ionization of these zinc vacancies reduces the average phosphor field slightly and reduces the phosphor field near the anode interface significantly.

Q-F_p and C-V analysis are then used to perform aging studies on ALE ZnS:Mn ACTFEL devices. From this experiment, the following observations can be made:

1) The interface state densities of the top and bottom interface are distinctly different and exhibit different aging characteristics.
2) Both shallow and deep traps are created during aging at the bottom interface.
3) A lesser number of predominately deep traps are created at the top interface during aging.
4) C_i decreases with aging time indicates that some of the interface state charge actually moves deeper into the ZnS bulk with aging.
5) The decrease in the C-V overshoot of the bottom interface indicates that the amount of space charge

build-up in the ZnS decreases with aging time. The C-V overshoot is evidence for the existence of space charge as discussed in chapter 4.

From these observations, an aging model for ALE ZnS:Mn ACTFEL devices is put forth to explain the cause for aging. This model explains the possible aging mechanisms for both interfaces as follows:

1) The asymmetry in the interface state density is attributed to the presence of Cl atom near the bottom interface; Cl is presumed to be present in a significantly lower concentration at the top interface. Cl_S is known to be relatively shallow donor in bulk ZnS. Therefore, Cl at the interface gives rise to shallow interface states.
2) <u>For the bottom interface</u>: The creation of shallow states at the bottom interface and movement of the charge centroid into the ZnS bulk is associated with the aging-induved migration of Cl away from the bottom interface into the ZnS bulk with aging time. The creation of deep interface states is due to the formation of V_S's at the interface which are formed as a result of Cl migration away from the bottom interface.
3) Cl migration away from the bottom interface with aging is responsible for the observed reduction in the build-up of space charge in the ZnS.

4) <u>For the top interface</u>: Aging trends are attributed to the creation of deeper interface states which arise from hot electron-induced atomic rearrangement at the interface. It is postulated that hot electron impingement and recombination at the top interface dislodges sulfur atoms, thus creating V_s's.

For future work, it is important to explore the following areas in which further understanding of ACTFEL device physics can be achieved:

1) Variations of the standard waveform of other ACTFEL devices that generate the basic three colors for full-color displays should be conducted. For example, preliminary electrical characterization of ALE Tb-doped green ACTFEL devices under various applied voltage waveforms yields completely different electrical trends compared to ALE ZnS:Mn ACTFEL devices.

2) Aging studies should also be conducted on other ACTFEL devices. For example, preliminary studies of ALE ZnS Tb-doped green ACTFEL devices indicate that the interface state densities are quite symmetrical and exhibit similar aging characteristics for both the top and bottom interfaces.

3) The issue of the existence and nature of space charge should be investigated by performing further electro-optic experiments on devices grown by ALE. ALE Tb-

doped green ACTFEL devices exhibit overshoots in the C-V and Q-F_p curves. This overshoot is found to occur at the top interface rather than at the bottom interface as the case for ALE ZnS:Mn ACTFEL devices.

4) SPICE modelling is recommended in order to better understand subtilities of the Q-F_p technique. This should be of particular help in attempts to understand devices exhibit space charge within the phosphor layer.

5) Temperature accelerated aging to measure thermal activation of Cl diffusion.

BIBLIOGRAPHY

1) C.N. King, Conference Record of the 1985 International Display Research Conference, San Diego (1985) p.155.

2) R. Tornqvist, Thesis, Helsinki University of Teaching, 1983, p.34.

3) B. Kazan Displays, 2 (1985) 85.

4) J. Davidson, Oregon State University, M.S Thesis, 1991.

5) R.C. McArthur, J.D. Davidson, J.F. Wager, I.Khormaei, and C.N. King, Appl.Phys. Lett. 56 (19), 1889, 1990.

6) J. Davidson, J.F. Wager, I. Khormaei, and C.N. King, ACTA Polytechnica Scandinavica 5th International Workshop on Electroluminescence 181, 1991.

7) A. Abu-Dayah, J.F. Wager, and S. Kobayashi, Appl. Phys. Lett. 62, 744 (1993).

8) S. Kobayashi, A. Abu-Dayah, and J.F. Wager, Electroluminescence, edited by V.P. Singh and J.C. McClure (El Paso, Cinco Puntos Press, 1992), p. 234.

9) A. Abu-Dayah, J.F. Wager, and S. Kobayashi, "Electrical Characterization of Atomic Layer Epitaxy, ZnS:Mn Alternating-Current Thin-Film Electroluminescent Devices Subject to Various Waveforms.", J. Appl. Phys. (submitted).

10) A. Abu-Dayah and J.F. Wager, "Aging studies of ZnS:Mn Alternating-Current Thin-Film Electroluminescent Devices Grown by Atomic Layer Epitaxy.", J.Appl. Phys. (submitted).

11) A. Abu-Dayah, J.F.Wager, and S. Kobayshi, "Electrical Characterization of ALE ZnS:Mn ACTFEL Devices.", SID 93 Digest, (accepted).

12) G. Destriau, J.Chem.Phys., 33 (1936) 587.

13) D. Kahng, Appl. Phys. Lett. 13 (1968) 210.

14) T. Inoguchi, M.Takeda, Y. Takahara, Y. Nakata and M. Yoshida, SID 74 Digest, 5 (1974) 84.

15) SID International Symposium, Planar Systems Vendor Display, 1991.

16) R.T. Tuenge, and J. Kane, "Bright Red El using a Thin-Film

Filter.", SID International Symposium Digest, 279, 1991.

17) G. Harkonen and H. Harkonen, "Green Emitting TFEL Device Grown by "ALE, SID International Symposium Digest, 13.1, 1990.

18) V. Shankar, S. Tanaka, M. Shiike, H. Deguchi, H. Kobayashi, and H. Sasakura, "Electroluminescence in Thin-Film CaS:Ce", Appl.Phys. Lett. 45 (1960), 1984.

19) Markku Leskela and Markku Tammenmaa, Materials Chemistry and Physics, 16 (1987) 349-371.

20) M.G. Clark, Proc. 9th Int. Vaccum Congr. & 5th Int. Conf. Solid surfaces, Madrid 1983, p. 499.

21) H. Kobayashi, S. Tanaka, V. Shankar, M. Shiiki, and H. Deguchi, J. Cryst. Growth, 72 (1985) 559.

22) H. Antson, M. Grasserbaur, M. Hamilo, L. Hiltunen, T. Kobayshi M. Leskela, L. Niisto, G. Stringer and Tammenmaa, Fresenius Z. Anal. Chem., 322 (1985) 165.

23) T. Suntola, J. Antson, A. Pakkala and S. Lindfors, SID 80 Digest, 11 (1980) 108.

24) V.-P. Tanninen, M. Oikkonen and T. Tuomi, Thin Solid Films, 109 (1983) 283.

25) J.F. Wager, A.A. Douglas, and D.C. Morton, Electroluminescence, edited by V.P. Singh and J.C. McClure (El Paso, Cinco Puntos Press, 1992), p.92.

26) J.D. Davidson, J.F. Wager, I. Khormaei, C.N. King, and R. Williams, IEEE Trans. Electron Devices ED-39, 1122 (1992).

27) R. Tornqvist and S. Korpela, J. Cryst. Growth 59, 395 (1982).

28) R. Khormaei, J.F. Wager, and C.N. King, SID 89 Dig. 20, p. 65 (1989)

29) R. Khormaei, C.N. King, R.E. Coovert, and J.F. Wager, SID 91 Dig. 22, p. 74 (1991).

30) J.D. Davidson, J.F. Wager, and S. Kobayashi, J. Appl. Phys. 71, 4040 (1992).

31) A. Mikami, K. Tareda, K. Okibayashi, K. Tanaka, M. Yoshida, and S. Nakajima, J. Appl. Phys. 72, 773 (1992).

32) A.A. Douglas, J.F. Wager, SID 92 Digest, 365 (1992).

33) A.A. Douglas, J.F. Wager, D.C. Morton, J.B. Koh, and C.P. Hogh, J. Appl. Phys. 73, 296 (1993).

34) P. Thioulouse, R. Tueta, A. Izrael, and N. Duruy, 1984 SID Proc. 15, p. 81 (1984).

35) Landolt-Bornstein, New Series (Springer, Berlin, 1987), Vol. 22a, p. 65.

36) E. Brinquier and A. Geoffroy, Appl. Phys. lett. 60, 1256 (1992).